

# Pivotal Role of Intersite Hubbard Interactions in Fe-doped $\alpha$ -MnO<sub>2</sub>

Ruchika Mahajan,<sup>†</sup> Arti Kashyap,<sup>†</sup> and Iurii Timrov<sup>\*,‡</sup>

<sup>†</sup>*School of Basic Sciences, Indian Institute of Technology Mandi, Himachal Pradesh  
175075, India*

<sup>‡</sup>*Theory and Simulation of Materials (THEOS), and National Centre for Computational  
Design and Discovery of Novel Materials (MARVEL), École Polytechnique Fédérale de  
Lausanne (EPFL), CH-1015 Lausanne, Switzerland.*

E-mail: [iurii.timrov@epfl.ch](mailto:iurii.timrov@epfl.ch)

## Abstract

We present a first-principles investigation of the structural, electronic, and magnetic properties of the pristine and Fe-doped  $\alpha$ -MnO<sub>2</sub> using density-functional theory with extended Hubbard functionals. The onsite  $U$  and intersite  $V$  Hubbard parameters are determined from first principles and self-consistently using density-functional perturbation theory in the basis of Löwdin-orthogonalized atomic orbitals. For the pristine  $\alpha$ -MnO<sub>2</sub> we find that the so-called C2-AFM spin configuration is the most energetically favorable, in agreement with the experimentally observed antiferromagnetic ground state. For the Fe-doped  $\alpha$ -MnO<sub>2</sub> two types of doping are considered: Fe insertion in the  $2 \times 2$  tunnels and partial substitution of Fe for Mn. We find that the interstitial doping preserves the C2-AFM spin configuration of the host lattice only when both onsite  $U$  and intersite  $V$  Hubbard corrections are included, while for the substitutional doping the onsite Hubbard  $U$  correction alone is able to preserve the C2-AFM spin configuration of the host lattice. The oxidation state of Fe is found to be

+2 and +4 in the case of the interstitial and substitutional doping, respectively, while the oxidation state of Mn is +4 in both cases. This work paves the way for accurate studies of other MnO<sub>2</sub> polymorphs and complex transition-metal compounds when the localization of 3d electrons occurs in the presence of strong covalent interactions with ligands.

# 1 Introduction

Manganese dioxide is an inexpensive and highly reactive material that has attracted great interest due to its structural diversity with different chemical and physical properties.<sup>1</sup> In particular,  $\alpha$ -MnO<sub>2</sub> is made up of  $2 \times 2$  channels due to edge and corner sharing of MnO<sub>6</sub> octahedra along the  $c$  axis, and there are two types of oxygen atoms having  $sp^2$  or  $sp^3$  hybridization (see Fig. 1). Such a tunnel-type structure generally can incorporate external cations (e.g. Li<sup>+</sup>, K<sup>+</sup>, NH<sub>4</sub><sup>+</sup>, Ba<sup>2+</sup>, Na<sup>+</sup>, Pb<sup>2+</sup>),<sup>2,3</sup> transition-metal elements (e.g. Ti, V, Cr, Fe, Co, Ni, Cu, Nb, Ru, Ag),<sup>4-10</sup> rare-earth elements (e.g. Ce),<sup>11</sup> and H<sub>2</sub>O molecules which can substantially alter its properties.  $\alpha$ -MnO<sub>2</sub> has very broad applications, e.g. it is used in Li-, Na-, and Mg-ion batteries,<sup>12-14</sup> Zn-air batteries, supercapacitors, electrochemical energy storage systems,<sup>15</sup> catalysts in water oxidation,<sup>16</sup> and many more.<sup>17,18</sup> Experimentally, it is reported to be a semiconductor<sup>19</sup> with an antiferromagnetic ordering below  $T_N = 24.5$  K, and it crystallizes in a tetragonal crystal structure with a space group  $I4/m$  (87).<sup>20</sup> Another experimental study showed that spin glass transition occurs in  $\alpha$ -MnO<sub>2</sub> at 50 K due to frustration.<sup>21-23</sup>

Many studies seek doping in  $\alpha$ -MnO<sub>2</sub> because it has large cavities. The doping enhances the stability of this material<sup>2-10</sup> and thus it allows for potential applications in the range from catalysts to energy storage systems. Generally, two types of doping are considered: *i*) the *interstitial* one, where the dopant is placed in the center of the  $2 \times 2$  tunnels, and *ii*) the *substitutional* one, where the dopant is partially substituted for Mn atoms.<sup>24</sup> Of particular interest is the Fe-doping of  $\alpha$ -MnO<sub>2</sub> because Fe atoms have an atomic radius

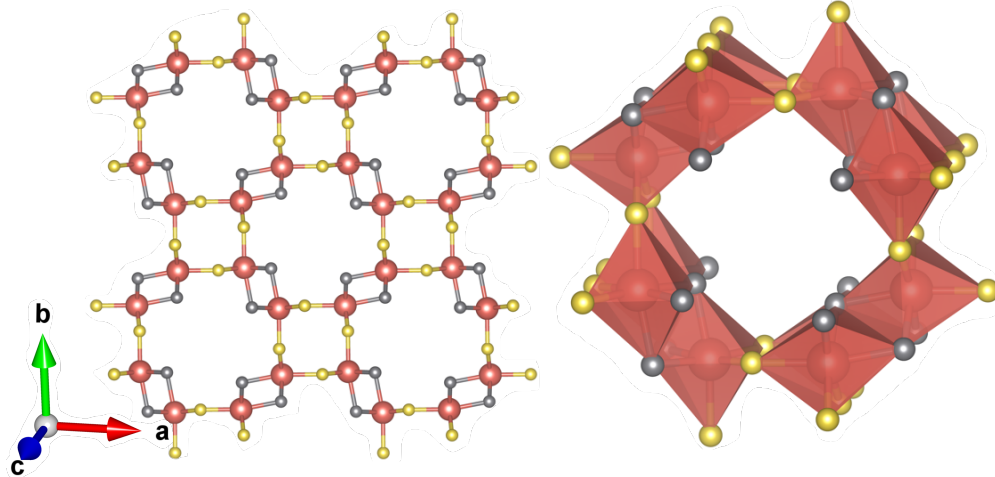


Figure 1: Experimental crystal structure of  $\alpha$ -MnO<sub>2</sub>.<sup>3</sup> Mn atoms are indicated in light brown color, while O atoms are indicated in yellow and gray to highlight two types of hybridizations,  $sp^2$  and  $sp^3$ , respectively. Rendered using VESTA.<sup>32</sup>

similar to the one of Mn atoms, and hence Fe can partially substitute Mn or it can easily fit into the cavity.  $\alpha$ -MnO<sub>2</sub> doped with Fe is used in industrial processes of preparing cyclohexanone by photocatalytic oxidation process of cyclohexane.<sup>25</sup> This compound is not only cheaper but also it shows highest photo-catalytic activity compared to other catalysts.<sup>25</sup> Moreover, Fe doping of  $\alpha$ -MnO<sub>2</sub> makes it better catalyst for oxygen evolution reaction and oxygen reduction reaction and an efficient electrode for Zn-air batteries.<sup>26</sup> However, despite numerous experimental studies of the Fe doping of  $\alpha$ -MnO<sub>2</sub><sup>24,27-30</sup> the understanding of the changes in the crystal structure, electronic and magnetic properties, and the oxidation state of Fe and Mn ions remains illusive. Only a few theoretical studies have attempted to shed more light on this problem<sup>29,31</sup> since the computational modeling of the pristine and Fe-doped  $\alpha$ -MnO<sub>2</sub> is very challenging due to a complex interplay between structural, electronic, and magnetic degrees of freedom.

First-principles simulations of the pristine and Fe-doped  $\alpha$ -MnO<sub>2</sub> using density-functional theory (DFT)<sup>33,34</sup> with local and semi-local exchange-correlation (xc) functionals encounter serious problems due to the presence of localized and partially-filled  $3d$  electrons. In particular, local spin-density approximation (LSDA) and spin-polarized generalized-gradient

approximation ( $\sigma$ -GGA) are unable to produce accurate results due to large self-interaction errors for  $3d$  electrons.<sup>35,36</sup> Therefore, more accurate approaches that go beyond standard DFT are needed. Many methods have been used to study  $\alpha$ -MnO<sub>2</sub> and most of them are based on Hubbard-corrected DFT (DFT+ $U$ <sup>37-39</sup>)<sup>14,40-43</sup> and DFT with hybrid functionals (e.g. HSE06<sup>44,45</sup>).<sup>41,42</sup> While for hybrid functionals the main bottlenecks are the high computational cost and difficulty to tune the amount of exact exchange, in DFT+ $U$  the value of the Hubbard  $U$  parameter is unknown and often it is chosen (semi-)empirically which possess ambiguities on the final results of interest. Alarmingly, the calibration procedure of  $U$  is highly arbitrary, which often results in incorrect interpretations of experiments, contradictory predictions, and generates a large spread in reported results.

Most DFT-based studies of  $\alpha$ -MnO<sub>2</sub> consider collinear spin configurations: the ferromagnetic (FM) and various types of the antiferromagnetic (AFM) orderings. In the AFM case, magnetic structures such as A2-AFM, C-AFM, C2-AFM, and G-AFM have been studied (see Fig. 2).<sup>10,16,40,41,46,47</sup> On the one hand, DFT with hybrid functionals predicts FM to be lower in energy than all types of the AFM configurations,<sup>41</sup> thus contradicting to the experimental observation of the AFM state.<sup>20</sup> On the other hand, DFT+ $U$  predicts different trends depending on the value of the Hubbard  $U$  parameter. In the vast majority of the DFT+ $U$  studies of  $\alpha$ -MnO<sub>2</sub>, the  $U$  parameter is chosen empirically in the range from 1 to 6 eV<sup>40,41,46</sup> such that DFT+ $U$  reproduces well some experimental property of interest (e.g., band gaps, magnetic moments, etc.). However, when selecting  $U$  empirically, it is often forgotten to pay attention also to the type of the Hubbard projectors that are used in various electronic-structure codes, as indeed the DFT+ $U$  results are extremely sensitive not only to the value of  $U$  but also to the type of these projectors.<sup>48-50</sup> Only in one DFT+ $U$  study of  $\alpha$ -MnO<sub>2</sub> so far the value of  $U$  was computed from first principles (using the constrained DFT),<sup>14</sup> though no information is provided regarding the magnetic ordering used. Therefore, a consistent comparison of the FM and various types of AFM orderings in the pristine and Fe-doped  $\alpha$ -MnO<sub>2</sub> using first-principles Hubbard parameters have not been performed so far. More-

over, in all previous Hubbard-corrected DFT studies only the onsite Hubbard  $U$  correction was included, while the intersite Hubbard interactions were fully disregarded even though they are known to be very important in  $\text{MnO}_2$  polymorphs due to strong  $\text{Mn}(3d)\text{-O}(2p)$  hybridization, as has been amply demonstrated in Ref. [50](#)

Herein, we present a fully first-principles study of the structural, electronic, and magnetic properties of the pristine and Fe-doped  $\alpha\text{-MnO}_2$  using DFT with extended Hubbard functionals (DFT+ $U$ + $V$ ).[51](#) The DFT+ $U$ + $V$  approach has proven to be effective for accurate description of various properties of solids and molecules.[20,50,52-59](#) We compute the onsite  $U$  and intersite  $V$  Hubbard parameters using density-functional perturbation theory (DFPT)[61,62](#) in the basis of Löwdin-orthogonalized atomic orbitals. Thus, we avoid any empiricism and ambiguities that are so common to the vast majority of other DFT+ $U$  studies. The Hubbard parameters are determined using the self-consistent procedure[53,62,63](#) to ensure the full consistency between the crystal and electronic structures. We find that C2-AFM is the most energetically favorable magnetic ordering in the pristine  $\alpha\text{-MnO}_2$  which agrees with the Goodenough-Kanamori rules.[64,65](#) Overall, the computed crystal structure parameters, band gaps, and magnetic moments are in good agreement with experiments. We find that the interstitial doping preserves the C2-AFM spin configuration of the host lattice only when both onsite  $U$  and intersite  $V$  Hubbard corrections are included, while for the substitutional doping the onsite Hubbard  $U$  correction alone is able to preserve the C2-AFM spin configuration of the host lattice. Finally, using the method of Ref. [66](#) we find that the oxidation state (OS) of Fe is +2 or +4 in the case of the interstitial and substitutional doping, respectively, while the OS of Mn is +4 irrespective of the doping type. These findings constitute a robust and reliable fully-first-principles characterization of the structural, electronic, and magnetic properties of the pristine and Fe-doped  $\alpha\text{-MnO}_2$  which can serve as a basis for further more advanced studies of this material.

The rest of the paper is organized as follows. Section [2](#) contains technical details of the calculations. In Sec. [3.1](#) we present our findings for the structural, electronic, and magnetic

properties of the pristine  $\alpha$ -MnO<sub>2</sub> for different types of collinear magnetic orderings, while Sec. 3.2 discusses our results for the Fe-doped  $\alpha$ -MnO<sub>2</sub>. In Sec. 4 we give our conclusions.

## 2 Computational details

All calculations were performed using the QUANTUM ESPRESSO package.<sup>67–69</sup> The computational method is described in Sec. S1 in supporting information (SI). For the pristine  $\alpha$ -MnO<sub>2</sub>, 5 collinear magnetic orderings are considered: FM, A2-AFM, C-AFM, C2-AFM, and G-AFM (see Fig. 2). The first 4 magnetic orderings have unit cells with 24 atoms, whereas G-AFM was modeled using a supercell of size  $1 \times 1 \times 2$  containing 48 atoms. For the Fe-doped  $\alpha$ -MnO<sub>2</sub>, also 5 collinear magnetic orderings are considered: interstitial (labeled as “A” and “D”) having 25 atoms and substitutional (“B”, “C”, and “E”) having 24 atoms in the simulation cell.

We have used the xc functional constructed using  $\sigma$ -GGA with the PBEsol prescription.<sup>70</sup> Pseudopotentials were chosen based on the SSSP library v1.1 (precision):<sup>71,72</sup> We have used `mn_pbesol_v1.5.uspp.F.UPF` (GBRV library v1.5<sup>73</sup>), `0.pbesol-n-kjpaw_ps1.0.1.UPF` and `Fe.pbesol-spn-kjpaw_ps1.0.2.1.UPF` (Pslibrary v0.3.1<sup>74</sup>). For metallic ground states, we used the Marzari-Vanderbilt (MV) smearing<sup>75</sup> with a broadening parameter of  $2 \times 10^{-2}$  Ry. The crystal structure for all spin configurations was optimized at three levels of theory (DFT, DFT+ $U$ , and DFT+ $U$ + $V$ ) using the Broyden-Fletcher-Goldfarb-Shanno (BFGS) algorithm<sup>76</sup> with the convergence thresholds of  $10^{-6}$  Ry,  $10^{-5}$  Ry/Bohr, and 0.5 KBar for the total energy, forces, and pressure, respectively. For structural optimizations, the  $\mathbf{k}$  points sampling of the first Brillouin zone was done using a uniform  $\Gamma$ -centered mesh of size  $4 \times 4 \times 12$  for all spin configurations except G-AFM for which a  $4 \times 4 \times 6$  mesh was used. Kohn-Sham wavefunctions and potentials were expanded in plane waves up to a kinetic-energy cutoff of 90 and 1080 Ry, respectively. Total energies, magnetic moments, band gaps, and the projected density of states (PDOS) were computed using denser  $\mathbf{k}$  points meshes of size  $8 \times 8 \times 24$  and

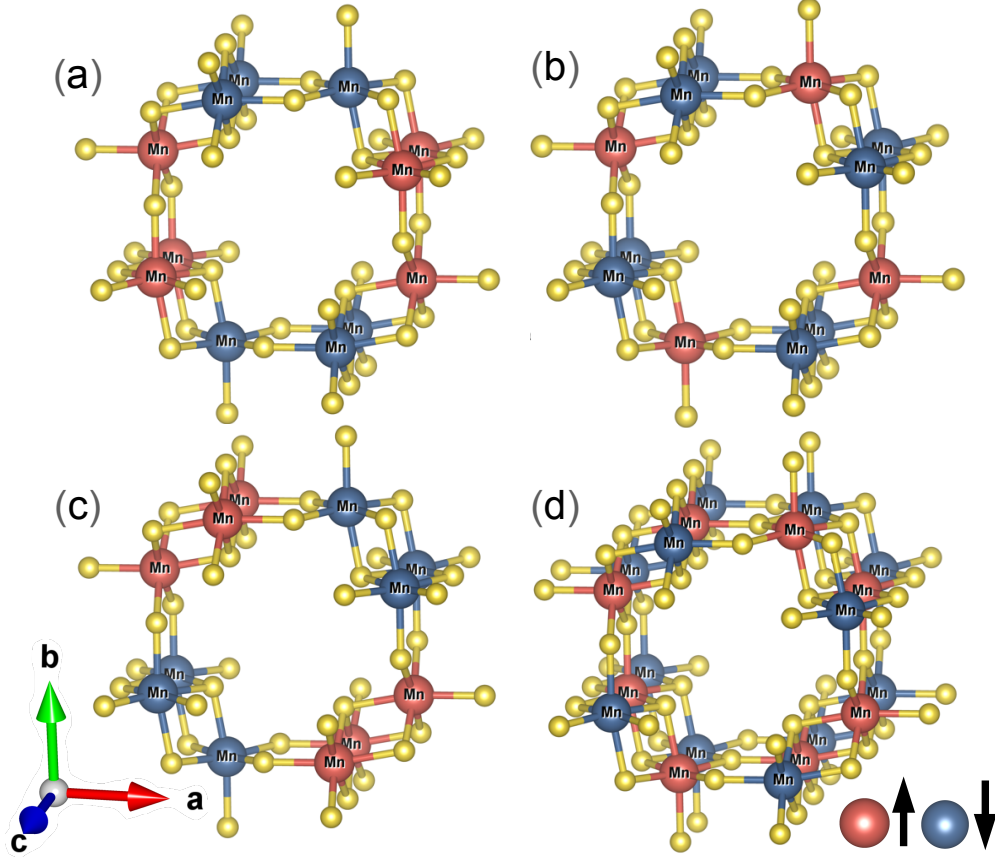


Figure 2: Four collinear AFM configurations of  $\alpha$ - $\text{MnO}_2$ : (a) A2-AFM, (b) C-AFM, (c) C2-AFM, and (d) G-AFM. Mn atoms with spin-up and spin-down alignments are shown in light brown and blue colors, respectively, while oxygen atoms are shown in yellow color. For FM, all Mn atoms have the same spin alignment (not shown). Rendered using VESTA.<sup>32</sup>

$8 \times 8 \times 12$ , respectively, and the Kohn-Sham wavefunctions and potentials were expanded using higher kinetic-energy cutoffs of 150 and 1800 Ry, respectively (to ensure a  $\sim 1$  meV accuracy when comparing the total energies). PDOS was plotted using a Gaussian smearing with a broadening parameter of  $4.4 \times 10^{-3}$  Ry.

DFT+ $U$  and DFT+ $U$ + $V$  calculations were performed using the Löwdin-orthogonalized atomic orbitals as Hubbard projector functions.<sup>77–80</sup> Hubbard  $U$  and  $V$  parameters were computed using DFPT<sup>61,62</sup> as implemented in the HP code<sup>81</sup> which is part of QUANTUM ESPRESSO. Hubbard parameters will be discussed in detail in the following. We have used uniform  $\Gamma$ -centered  $\mathbf{k}$  and  $\mathbf{q}$  points meshes of size  $2 \times 2 \times 6$  and  $1 \times 1 \times 3$ , respectively, for all spin configurations (for the pristine and Fe-doped  $\alpha$ - $\text{MnO}_2$ ) except G-AFM for which we

have used  $\mathbf{k}$  and  $\mathbf{q}$  points meshes of size  $2 \times 2 \times 4$  and  $1 \times 1 \times 2$ , respectively. Kohn-Sham wavefunctions and potentials were expanded in plane waves up to a kinetic-energy cutoff of 60 and 720 Ry, respectively, giving the accuracy of computed Hubbard parameters of  $\sim 0.01$  eV. It is important to stress that we have used a self-consistent procedure for the calculation of  $U$  and  $V$  as described in detail in Ref.<sup>62</sup> which consists of cyclic calculations containing structural optimizations and recalculations of Hubbard parameters for each new geometry.

The data used to produce the results of this paper are available in the Materials Cloud Archive.<sup>82</sup>

## 3 Results and Discussion

### 3.1 Pristine $\alpha$ -MnO<sub>2</sub>

In this section we present our findings for the pristine  $\alpha$ -MnO<sub>2</sub>. First we discuss the computed Hubbard parameters, and then we analyze the structural, magnetic, and electronic properties of this material.

#### 3.1.1 Hubbard parameters

In previous studies it was shown that the values of Hubbard parameters depend on a type of Hubbard projectors, pseudopotentials, oxidation state of transition-metal elements, xc functional, chemical environment, etc.<sup>49,50,83–85</sup> In particular, in Ref.<sup>50</sup> it is shown for  $\beta$ -MnO<sub>2</sub> that the values of Hubbard  $U$  parameters for Mn( $3d$ ) states differ by 1.4 – 2.2 eV depending on whether nonorthogonalized or orthogonalized atomic orbitals are used as Hubbard projector functions. Since it was concluded that the highest accuracy is achieved when using orthogonalized atomic orbitals, here we present results obtained using this type of Hubbard projectors.

Table 1 shows self-consistent Hubbard parameters for five collinear magnetic configura-



Table 1: Self-consistent Hubbard parameters (HP) in eV computed using DFPT for five magnetic orderings of the pristine  $\alpha$ -MnO<sub>2</sub>: FM, A2-AFM, C-AFM, C2-AFM, and G-AFM. The onsite  $U$  for Mn( $3d$ ) states and intersite  $V$  between Mn( $3d$ ) and O( $2p$ ) states are computed in the frameworks of DFT+ $U$  and DFT+ $U$ + $V$  (PBEsol functional) using Löwdin-orthogonalized atomic orbitals as Hubbard projector functions.

Method	HP	Magnetic ordering				
		FM	A2-AFM	C-AFM	C2-AFM	G-AFM
DFT+ $U$	$U$	6.67	6.53	6.41	6.47	6.43
DFT+ $U$ + $V$	$U$	6.83	6.74	6.65	6.67	6.73
	$V$	0.72 – 1.09	0.75 – 1.07	0.71 – 1.12	0.66 – 1.13	0.76 – 1.16

tions of  $\alpha$ -MnO<sub>2</sub> (FM, A2-AFM, C-AFM, C2-AFM, and G-AFM) computed using DFPT in the basis of Löwdin-orthogonalized atomic orbitals as described in Sec. S1 in SI. As in the case of  $\beta$ -MnO<sub>2</sub>, for  $\alpha$ -MnO<sub>2</sub> we find that the value of Hubbard  $U$  varies marginally depending on the type of the magnetic ordering. When using the extended formulation of DFT+ $U$  by incorporating also intersite  $V$ , the value of  $U$  increases slightly due to changes in the electronic screening. In practice, in the DFT+ $U$ + $V$  framework the size of the response matrices  $\chi$  and  $\chi_0$  is larger than in the DFT+ $U$  case because we compute the response not only of Mn( $3d$ ) states but also of O( $2p$ ) states. Hence, when inverting these response matrices there is a mixing of all matrix elements including those that describe a coupling of Mn( $3d$ ) and O( $2p$ ) states, and the final values of  $U$  and  $V$  are obtained according to Eq. (S4) in SI.

As can be seen in Table 1, the intersite Hubbard  $V$  parameters are smaller than the onsite Hubbard  $U$  by a factor of 6 – 9. Nevertheless, the relatively small  $V$  values turn out to be important to improve the accuracy of various ground-state properties of  $\alpha$ -MnO<sub>2</sub> as will be shown in the following, in analogy with findings for  $\beta$ -MnO<sub>2</sub>.<sup>50</sup>

### 3.1.2 Structural properties

$\alpha$ -MnO<sub>2</sub> has a tetragonal crystal structure which is described by two lattice parameters  $a$  and  $c$ .<sup>20</sup> The detailed comparison of these lattice parameters and the cell volume  $V$  at three levels

of theory and for different magnetic orderings is presented in Table S1 in SI, while here we discuss briefly only the general trends. DFT underestimates the  $a$  parameter, while  $c$  is very close to the experimental value, and hence overall the cell volume is also underestimated by 3–4 %. In contrast, adding the Hubbard  $U$  correction leads to  $a$  and  $c$  which are larger than the experimental ones, and the cell volume is overestimated by 3–6 %. The best agreement with the experiments is achieved at the level of DFT+ $U$ + $V$ : the optimized  $a$  parameter falls in the range of experimental values or slightly overestimated, while  $c$  is also slightly overestimated, and the cell volume is within 1–3 % compared to experiments. Within DFT+ $U$ + $V$ , three types of magnetic orderings (C-AFM, C2-AFM, and G-AFM) give the most accurate predictions of the lattice parameters and the cell volume. Importantly, at all levels of theory we find that the cell remains tetragonal in agreement with experiments and in contrast to previous works that reported a small monoclinic distortion.<sup>40,41</sup> Such a discrepancy with respect to previous theoretical studies could be due to the fact that in this work we use more stringent computational setup when performing structural optimizations.

To be more specific, we focus on the C2-AFM ordering that was also studied in detail in previous works<sup>40,41</sup> and because this is the most energetically favorable ordering as will be shown in Sec. 3.1.3. Table 2 summarizes the crystal structure parameters, bond lengths and angles for this spin configuration that were optimized at the levels of DFT, DFT+ $U$ , and DFT+ $U$ + $V$  and as measured in experiments. It can be seen that the most accurate agreement with experiments is achieved using DFT+ $U$ + $V$ . In particular, when using DFT+ $U$ + $V$  we find two values of bond lengths consistently with experiments, while when using DFT and DFT+ $U$  there are some variations in bond lengths due to lowering of the symmetry. These findings underline the importance not only of the onsite Hubbard corrections but also of the intersite ones when optimizing the crystal structure and atomic positions for the pristine  $\alpha$ -MnO<sub>2</sub>. In the following sections we present various ground-state properties of the pristine  $\alpha$ -MnO<sub>2</sub> computed at different levels of theory and for different magnetic orderings using respective crystal structure parameters.

Table 2: Comparison of experimental and theoretical (computed for C2-AFM using DFT, DFT+ $U$ , and DFT+ $U+V$ ) crystal structure parameters (CSP) for the pristine  $\alpha$ -MnO<sub>2</sub> [see Fig. 2 (c)]: the lattice parameters  $a$  and  $c$  (in Å), the cell volume  $V$  (in Å<sup>3</sup>), the bond lengths  $d_1$  and  $d_2$  (in Å), and the bond angles  $\theta_1$  and  $\theta_2$ . DFT and DFT+ $U$  structures have lower symmetry, hence the bond lengths  $d_1$  (and  $d_2$ ) take multiple values.

CSP	DFT	DFT+ $U$	DFT+ $U+V$	Expt.
$a$	9.66	9.85	9.78	9.75 <sup>a</sup> , 9.79 <sup>c</sup> , 9.84 <sup>b</sup>
$c$	2.83	2.93	2.91	2.86 <sup>a,b</sup> , 2.87 <sup>c</sup>
$V$	263.9	284.6	278.3	272.0 <sup>a</sup> , 274.5 <sup>c</sup> , 276.9 <sup>b</sup>
$d_1$	1.85, 1.87	1.90, 1.92	1.90	1.89 <sup>d</sup>
$d_2$	1.88, 1.91	1.94	1.93	1.93 <sup>d</sup>
$\theta_1$	131.0	129.5	129.8	130.2 <sup>e</sup>
$\theta_2$	98.0	98.6	98.3	98.2 <sup>e</sup>

<sup>a</sup>Ref. <sup>2</sup>   <sup>b</sup>Ref. <sup>86</sup>   <sup>c</sup>Ref. <sup>87</sup>   <sup>d</sup>Ref. <sup>88</sup>   <sup>e</sup>Refs. <sup>26</sup>

### 3.1.3 Energetics

Experimentally it is known that the pristine  $\alpha$ -MnO<sub>2</sub> has an AFM ordering below the Néel temperature of 24.5 K,<sup>20</sup> however the precise direction of the atomic magnetic moments is not known. In this respect, computational studies based on DFT could be useful as they might suggest what type of the magnetic ordering is the most energetically favorable. In particular, DFT+ $U$  predictions are very sensitive not only to the value of  $U$  but also to the type of Hubbard projector functions. For example, in Ref. <sup>41</sup> it is reported that for the effective  $U \geq 2.0$  eV and when using nonorthogonalized atomic orbitals as Hubbard projector functions the FM ordering is the most energetically favorable compared to all types of the AFM ordering. In contrast, in Refs. <sup>42,46,89</sup> it was found that FM is the most energetically favorable for the effective  $U \gtrsim 4.0$  eV and when using projector augmented wave (PAW) Hubbard projectors. In this work we do not use empirical values of  $U$  contrary to previous works, and hence here we do not provide ranges of  $U$  for which FM or AFM is the most energetically favorable. Instead, we use first-principles Hubbard parameters reported in Table 1 respectively for each spin configuration and check which one has the lowest energy. We use exactly the same approach as in Ref. <sup>50</sup> for  $\beta$ -MnO<sub>2</sub> (in particular, see the discussion

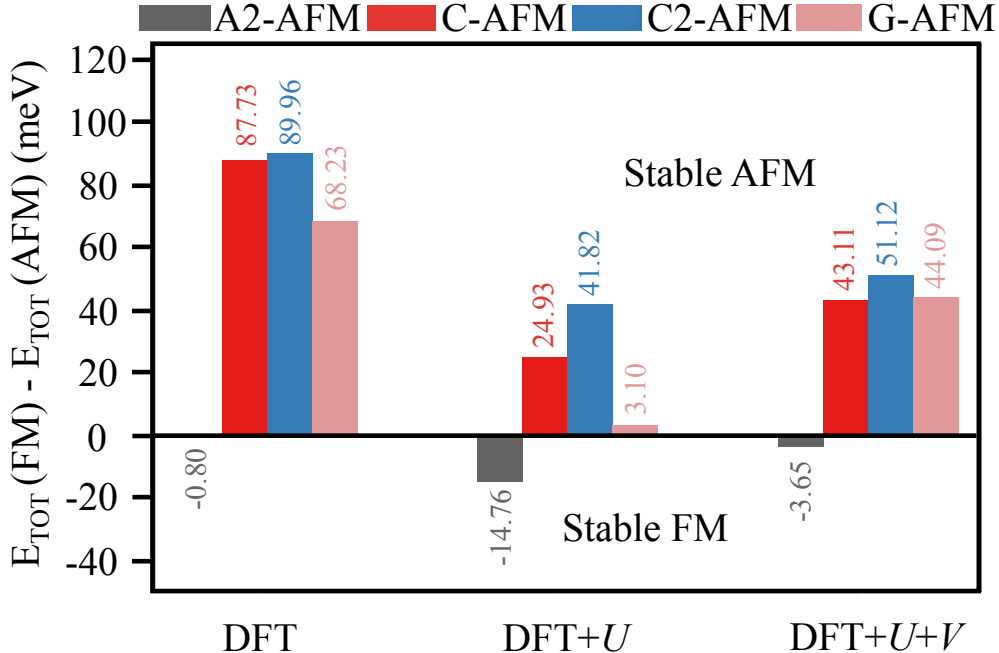


Figure 3: Total energy difference per formula unit (in meV) for five collinear magnetic orderings of the pristine  $\alpha$ -MnO<sub>2</sub> (FM, A2-AFM, C-AFM, C2-AFM, G-AFM) computed at three levels of theory (DFT, DFT+ $U$ , and DFT+ $U$ + $V$ ) using the PBEsol functional. For each case, the Hubbard parameters  $U$  and  $V$  were computed using DFPT and Löwdin-orthogonalized atomic orbitals, and they are listed in Table 1. Positive values on the plot mean that the AFM ordering is lower in energy than FM and hence the former is more energetically favorable, while negative values mean the opposite. The largest positive value on the plot (at each level of theory) corresponds to the lowest-energy magnetic ordering.

in Sec. IV C of Ref. <sup>50</sup>). Interestingly, we find that using our first-principles values of Hubbard parameters ( $U \approx 6 - 7$  eV and  $V \approx 0.7 - 1.2$  eV, see Table 1) and Löwdin-orthogonalized atomic orbitals, three types of the AFM ordering (C-AFM, C2-AFM, and G-AFM) are more energetically favorable than the FM one (see Fig. 3). This finding clearly shows that the choice of Hubbard projector functions is as crucial as the values of Hubbard parameters, and hence both should be considered when comparing conclusions from different works. However, one should keep in mind that there are also other differences between this work and previous studies, such as e.g. different pseudopotentials, which could also affect the final DFT+ $U$ (+ $V$ ) predictions. <sup>49</sup>

As can be seen in Fig. 3, C2-AFM is the most energetically favorable spin configuration at all levels of theory. However, at the levels of DFT+ $U$  and DFT+ $U$ + $V$ , C2-AFM

has larger energy difference compared to C-AFM and G-AFM. This shows that Hubbard-corrected DFT stabilizes C2-AFM more than standard DFT. It is noteworthy that DFT+ $U$  and DFT+ $U+V$  convey similar trends for the energetics of the pristine  $\alpha$ -MnO<sub>2</sub>, hence the intersite  $V$  corrections turn out to be no so crucial contrary to what is the case for  $\beta$ -MnO<sub>2</sub>.<sup>50</sup> However, it will be shown in the following that for the Fe-doped  $\alpha$ -MnO<sub>2</sub> the intersite Hubbard corrections are crucial to stabilize the C2-AFM spin configuration of the host lattice. Finally, we note that the C2-AFM ordering is consistent with the Goodenough-Kanamori rules,<sup>64,65</sup> which state that superexchange interactions favor AFM coupling when the Mn-3*d* and O-2*p* orbitals overlap as in a linear (180°) Mn–O–Mn group (point sharing of MnO<sub>6</sub> octahedra, see Fig. 1), while they favor FM coupling when the Mn-3*d* and O-2*p* orbitals overlap as in a bent (90°) Mn–O–Mn group (edge sharing of MnO<sub>6</sub> octahedra, see Fig. 1).<sup>46</sup> Even though the bond angles are not 90° and 180° as required by the Goodenough-Kanamori rules (see Table 2), we still find that C2-AFM is the most energetically favorable magnetic ordering.

### 3.1.4 Magnetic moment

Figure 4 shows a comparison of the magnetic moments on Mn atoms in the pristine  $\alpha$ -MnO<sub>2</sub> as measured in experiments and as computed using three levels of theory for five magnetic orderings. The magnetic moments were determined using the projection method, i.e. by computing the onsite occupation matrix ( $I = J$ ) using Eq. (S3) in SI and then by taking a difference between the spin-up and spin-down components. It can be seen in Fig. 4 that DFT underestimates the magnetic moments by about 29 – 36% depending on the type of the magnetic ordering. DFT+ $U$  provides the closest agreement with experiments with magnetic moments being underestimated by 6 – 15%, while DFT+ $U+V$  gives magnetic moments that fall in the range between the DFT and DFT+ $U$  predictions. This result is not surprising, since the onsite  $U$  correction localizes the 3*d* electrons on the Mn atoms and reduces the hybridization with the ligand states, and thus the magnetic moments are increased. Instead,

within DFT+ $U$ + $V$  the hybridization with ligands is partially restored while still preserving the localized nature of the 3d electrons, and as a consequence the magnetic moments are slightly decreased.

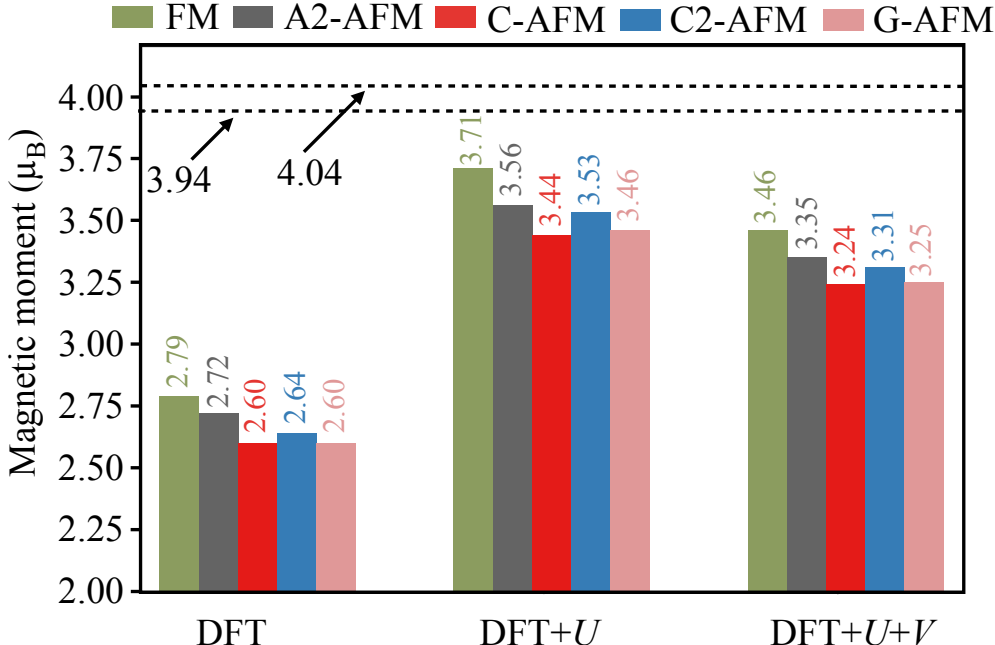


Figure 4: Magnetic moment (in  $\mu_B$ ) on Mn atoms in the pristine  $\alpha$ -MnO<sub>2</sub> for five collinear magnetic orderings (FM, A2-AFM, C-AFM, C2-AFM, G-AFM) computed at three levels of theory (DFT, DFT+ $U$ , and DFT+ $U$ + $V$ ) using the PBEsol functional. For each case, the Hubbard parameters  $U$  and  $V$  were computed using DFPT and are listed in Table 1. The experimental magnetic moments are 3.94 – 4.04  $\mu_B$ <sup>90</sup> and 4.04  $\mu_B$ <sup>22</sup> and they are indicated with horizontal dashed lines.

For our best candidate (i.e. C2-AFM) with our best approach (DFT+ $U$ + $V$ ) the computed magnetic moment is 3.31  $\mu_B$  which differs from the experimental ones by 16 – 18%. Thus, there is definitively a room for improvements, and this could be possibly achieved by including also the Hund’s  $J$  interactions,<sup>91–93</sup> but this goes beyond the frames of this study.

### 3.1.5 Band gap

Pristine  $\alpha$ -MnO<sub>2</sub> is a semiconductor, but the exact value of the band gap is difficult to determine experimentally since it is hard to synthesize pure samples without dopants. Noticeable works are Refs.<sup>19,94,95</sup> that reported experimental band gap values in the range from 1.61

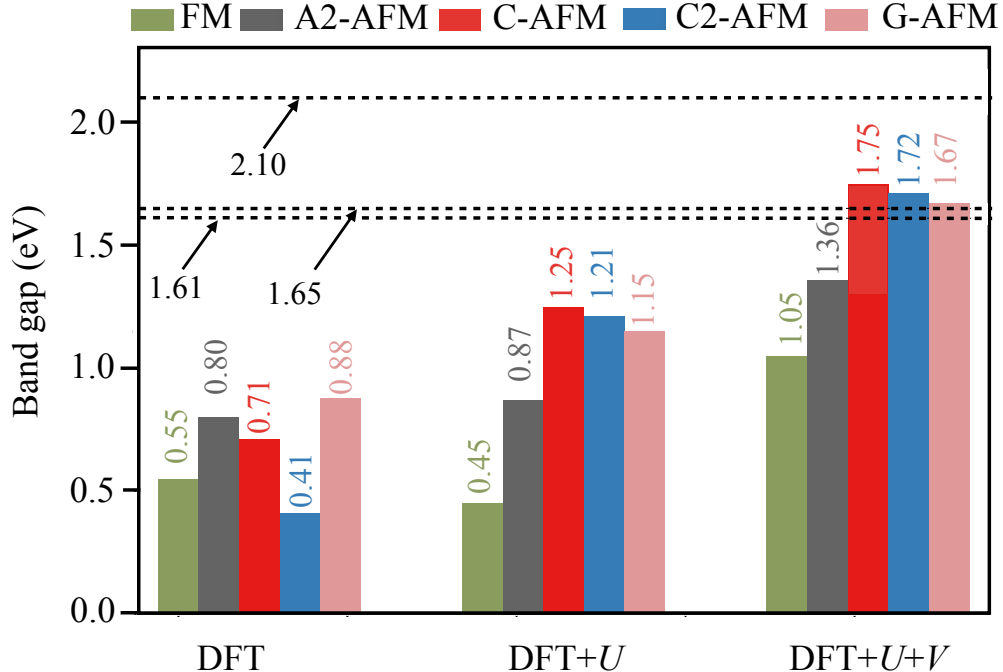


Figure 5: Band gap (in eV) in the pristine  $\alpha$ -MnO<sub>2</sub> for five collinear magnetic orderings (FM, A2-AFM, C-AFM, C2-AFM, G-AFM) computed at three levels of theory (DFT, DFT+U, and DFT+U+V) using the PBEsol functional. The experimental band gaps (1.61 eV,<sup>19</sup> 1.65 eV,<sup>94</sup> and 2.10 eV<sup>95</sup>) are indicated with horizontal dashed lines.

to 2.10 eV. Previous computational studies reported quite scattered values of band gaps depending on the method used. For example, in Ref.<sup>41</sup> the HSE06 functional was used that predicted FM as the ground state with the respective band gap of 2.2 eV. In the same work, the authors used DFT+U with the empirical  $U = 1.6$  eV and nonorthogonalized atomic orbitals as Hubbard projectors predicting C2-AFM to be the most energetically stable with a band gap of 0.94 eV. In another DFT+U study,<sup>40</sup> empirical  $U = 2.8$  eV and  $J = 1.2$  eV with PAW Hubbard projectors were used giving the band gap of 1.33 eV for C2-AFM. Finally, in the DFT+U study of Ref.<sup>96</sup> the empirical  $U = 3.9$  eV with PAW Hubbard projectors was used for C2-AFM giving the gap of 0.70 eV. Hence, in all these studies the band gap values lie outside the experimental range.

Figure 5 shows a comparison of band gaps computed using DFT, DFT+U, and DFT+U+V for five magnetic orderings of the pristine  $\alpha$ -MnO<sub>2</sub>. We can see that on average DFT underestimates the band gaps the most, followed by DFT+U and then by DFT+U+V. As in

the case of  $\beta$ -MnO<sub>2</sub>, the band gap is very sensitive to the type of the magnetic ordering.<sup>50</sup> Here we find that DFT+ $U$ + $V$  again provides the most accurate band gaps, with C-AFM, C2-AFM, and G-AFM having band gaps that fall in the range of the experimental values. In particular, the band gap for the C2-AFM ordering, which is the most energetically favorable, is 1.72 eV which is very close to the lower bound of the known experimental values (1.61 – 1.65 eV). Definitely, the narrowing down of the experimental range of band gaps is needed in order to further assess the predictive accuracy of DFT+ $U$ + $V$  - this requires further experimental scrutiny.

### 3.1.6 Projected density of states

Figure 6 shows the spin-resolved PDOS and total DOS for the FM and C2-AFM magnetic orderings of the pristine  $\alpha$ -MnO<sub>2</sub> computed at three levels of theory, while in Fig. S1 in SI we show the spin-resolved PDOS for the other three AFM magnetic orderings. The spin-up (upper part) and spin-down (lower part) components of the PDOS are shown on each panel in Fig. 6 and they were obtained by summing over all atoms of the same type. Mn1 and Mn2 correspond to Mn atoms with the opposite spin polarizations in the AFM case. In general, the trends for  $\alpha$ -MnO<sub>2</sub> are very similar to those that were observed for  $\beta$ -MnO<sub>2</sub>.<sup>50</sup>

In the DFT case, we see that the Mn(3*d*) states are very delocalized due to large self-interaction errors, and they hybridize strongly with the O(2*p*) states. The exact shape of the PDOS varies depending on the type of magnetic ordering. However, qualitatively the PDOS for various AFM types are very similar and differ mainly by the magnitude of the band gap and details in the dispersion of the valence and conduction bands. The top of the valence bands is of a mixed Mn(3*d*) and O(2*p*) character, while the bottom of the conduction bands is dominated by the Mn(3*d*) states.

The PDOS at the DFT+ $U$  level of theory differs strongly from the DFT one. As in the case of  $\beta$ -MnO<sub>2</sub>, the application of the Hubbard  $U$  correction pushes the occupied Mn(3*d*) states to lower energies while the empty Mn(3*d*) states are pushed to higher energies. As



a consequence, the top of the valence bands becomes of a pure  $O(2p)$  character, while the bottom of the conduction bands becomes of a mixed  $Mn(3d)$  and  $O(2p)$  character. As in Ref. <sup>41</sup> we find that for FM the empty  $e_g$  states in the spin-up channel overlap with the empty  $t_{2g}$  and  $e_g$  states in the spin-down channel in the DFT case, while in DFT+ $U$  these empty states in the spin-down channel are shifted to higher energies and there is an energy gap between these states and the empty  $e_g$  states in the spin-up channel. For AFM, the trends are the same and they apply to Mn1 and Mn2 atoms that have opposite spin polarizations. Finally, within DFT+ $U$ + $V$  the PDOS looks very similar to the one computed using DFT+ $U$ . One of the major differences is that the band gap is larger in DFT+ $U$ + $V$  than in DFT+ $U$ , as discussed in Sec. 3.1.5 and the energy separation between the groups of empty bands is somewhat smaller in DFT+ $U$ + $V$ .

We are not aware of any valence- or conduction-band spectra measured in the X-ray photoelectron spectroscopy (XPS) and X-ray absorption near-edge structure (XANES) experiments for the pristine  $\alpha$ - $MnO_2$ . Hence, at this stage we cannot verify the accuracy of the computed spin-polarized PDOS. However, these results are valuable for further discussions when considering the Fe-doped  $\alpha$ - $MnO_2$ . In particular, our goal is to understand where the  $Fe(3d)$  states are located and whether the semiconducting character of  $\alpha$ - $MnO_2$  is preserved after doping. All this is discussed in Sec. 3.2.5.

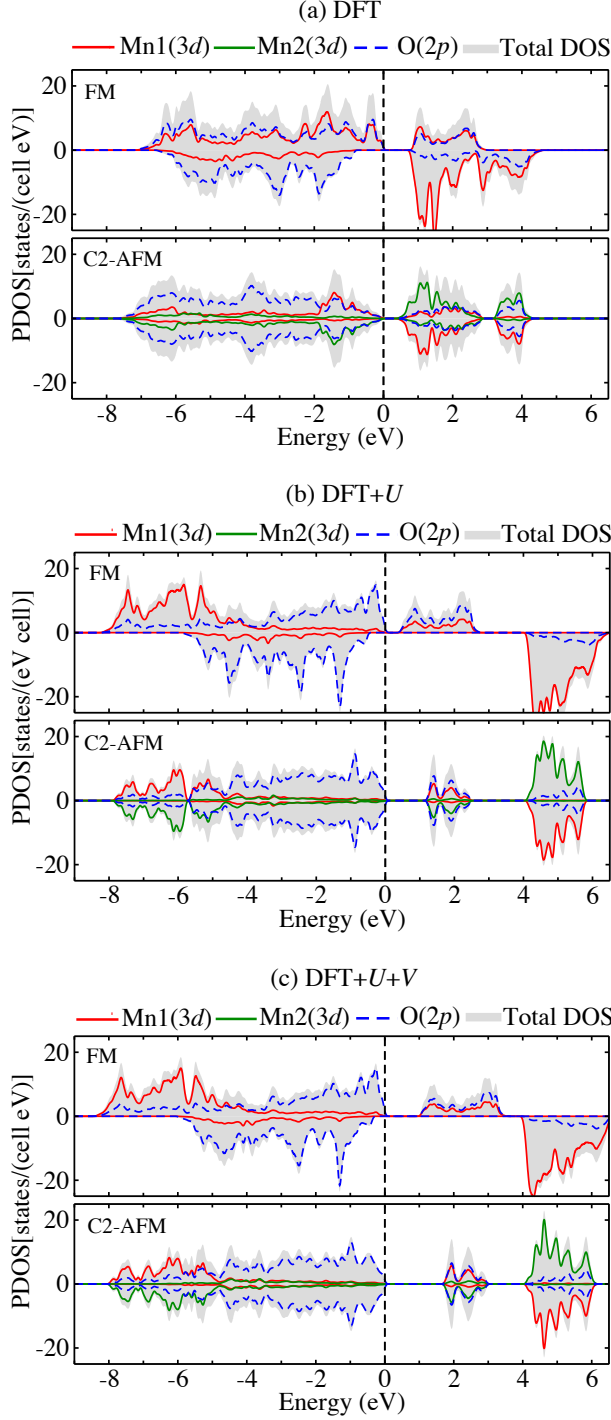


Figure 6: Spin-resolved PDOS and total DOS for the FM and C2-AFM magnetic orderings of the pristine  $\alpha$ - $\text{MnO}_2$  computed at three levels of theory using the PBEsol functional: (a) DFT, (b) DFT+ $U$ , and (c) DFT+ $U$ + $V$ . For each case, the Hubbard parameters  $U$  and  $V$  were computed using DFPT using Löwdin-orthogonalized atomic orbitals and are listed in Table 1. The zero of energy corresponds to the top of the valence bands.

## 3.2 Fe-doped $\alpha$ -MnO<sub>2</sub>

In this section we discuss structural, electronic, and magnetic properties of the Fe-doped  $\alpha$ -MnO<sub>2</sub>. We examine two types of doping, namely the interstitial one (FeMn<sub>8</sub>O<sub>16</sub>) and the substitutional one (FeMn<sub>7</sub>O<sub>16</sub>). For the former case we consider two spin configurations (labeled as “A” and “D”), while for the latter we consider three cases (“B”, “C”, and “E”). These spin configurations are based on the C2-AFM and FM magnetic orderings of the pristine  $\alpha$ -MnO<sub>2</sub>, since the former is the most energetically favorable one while the latter is also often considered in various studies. All these five cases of Fe-doped  $\alpha$ -MnO<sub>2</sub> differ by the variations in the chemical environment and magnetic interactions for Fe atoms and are schematically represented in Fig. 7. We also note that the configurations A, B, and C have the FM ordering, while D and E have the ferrimagnetic (FiM) ordering.

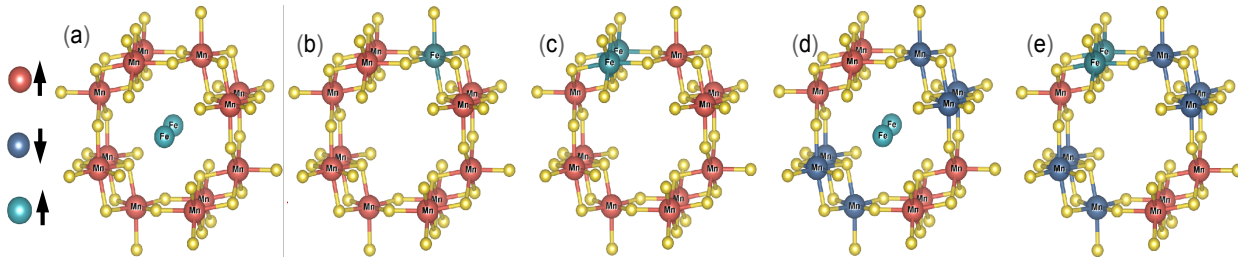


Figure 7: Five collinear spin configurations for the Fe-doped  $\alpha$ -MnO<sub>2</sub>: (a) A, (b) B, (c) C, (d) D, and (e) E. A and D correspond to the interstitial doping, while B, C, and E correspond to the substitutional doping. Light brown and blue colors correspond to Mn atoms with spin-up and spin-down alignments, respectively, while light green color corresponds to the Fe atom with the spin-up alignment. The oxygen atoms are shown in yellow color. Rendered using VESTA.<sup>32</sup>

### 3.2.1 Hubbard parameters

In the previous DFT+ $U$  studies of the Fe-doped  $\alpha$ -MnO<sub>2</sub>,<sup>29,31</sup> the value of Hubbard  $U$  for Mn(3d) states was chosen empirically and it was assumed to be exactly the same as in the pristine  $\alpha$ -MnO<sub>2</sub>. Here we show that when  $U$  is computed from first principles, its value for Mn(3d) states changes due to the Fe doping, since the latter leads to changes in the crystal and electronic structure. Indeed, from Table 3 we can see that on average the  $U$  parameter

Table 3: Self-consistent Hubbard parameters (HP) in eV computed using DFPT for five magnetic orderings of the Fe-doped  $\alpha$ -MnO<sub>2</sub>: A, B, C, D, and E. The onsite  $U$  for Mn(3d) and Fe(3d) states and intersite  $V$  for Mn(3d)–O(2p) and Fe(3d)–O(2p) interactions are computed in the frameworks of DFT+ $U$  and DFT+ $U$ + $V$  (PBEsol functional) using Löwdin-orthogonalized atomic orbitals as Hubbard projector functions.

Method	HP	Atoms	Magnetic ordering				
			A	B	C	D	E
DFT+ $U$	$U$	Mn	7.01 – 7.10	6.65 – 6.72	6.65 – 6.72	6.54 – 7.02	6.46 – 6.48
		Fe	5.92	6.03	6.02	5.58	5.94
DFT+ $U$ + $V$	$U$	Mn	7.24 – 7.60	6.85 – 6.95	6.88 – 6.96	6.78 – 7.37	6.62 – 6.73
		Fe	5.86	6.95	6.94	5.69	6.58
	$V$	Mn–O	0.82 – 1.23	0.75 – 1.16	0.75 – 1.18	0.69 – 1.25	0.64 – 1.18
		Fe–O	0.53	1.03 – 1.37	1.05 – 1.37	0.54 – 0.63	0.75 – 1.28

for Mn(3d) states is increased by a fraction of an eV compared to the pristine  $\alpha$ -MnO<sub>2</sub> case (cf. Table 1). Moreover, there is no longer just one global value of  $U$  for all Mn sites in the structure, instead there are slightly different  $U$  values for different Mn sites. This is so because the insertion of Fe in the  $\alpha$ -MnO<sub>2</sub> host lattice leads to structural distortions which break the equivalence of the Mn sites. This approach was also used in Refs.<sup>54,97</sup> to determine the self-consistent site-dependent Hubbard parameters in perovskites due to the presence of oxygen vacancies.

The Hubbard  $U$  parameter for Fe(3d) states is in the range from roughly 5.6 to 7.0 eV depending on the method used (DFT+ $U$  or DFT+ $U$ + $V$ ) and on the type of the spin configuration. These values are larger than the value of 5.1 eV which is obtained for the bulk Fe. This shows once again that  $U$  is not transferable and it is sensitive to changes in the chemical environment and magnetic interactions.

The intersite Hubbard  $V$  parameters for the Mn–O and Fe–O couples are also listed in Table 3. We can see that  $V$  for Mn–O did not change substantially with respect to  $V$  values in the pristine  $\alpha$ -MnO<sub>2</sub> case, and they span approximately the same range. Moreover, the  $V$  values for Fe–O are similar to those for Mn–O. In order to assess the importance of intersite Hubbard corrections for the Fe-doped  $\alpha$ -MnO<sub>2</sub>, in the following we present the

ground-state properties computed using DFT+ $U$  and DFT+ $U+V$  with the respective sets of self-consistent site-dependent Hubbard parameters.

### 3.2.2 Structural properties

Doping of  $\alpha$ -MnO<sub>2</sub> with Fe leads to structural distortions (see Table S2 in SI). From our calculations we find that in the case of A type doping the lattice preserves the tetragonal symmetry at all levels of theory, while for the B, C, and D types of doping the lattice has a very small monoclinic distortion. In the case of the E type doping, the optimized structure has a triclinic cell at the levels of DFT+ $U$  and DFT+ $U+V$ , while at the DFT level the cell is monoclinic. We are aware of only one experimental study of the Fe-doped  $\alpha$ -MnO<sub>2</sub><sup>29</sup> showing that the lattice preserves the tetragonal symmetry like in the pristine  $\alpha$ -MnO<sub>2</sub>. This seems to suggest that the A type is the most likely spin configuration in the case of the interstitial doping. However, in order to understand better this aspect, further high-resolution experimental investigations of different types of doping of  $\alpha$ -MnO<sub>2</sub> are needed in order to detect possible monoclinic (or triclinic) distortions.

For what concerns the crystal structure parameters, we also observe different trends. In the case of the interstitial doping (A and D), Fe atoms residing in the centers of the  $2 \times 2$  channels form bonds with the nearest four O atoms (see Fig. S2 in SI). Our calculations show that this leads to the reduction of the  $a$  and  $b$  lattice parameters by  $\sim 2\%$  with respect to the pristine  $\alpha$ -MnO<sub>2</sub> case, while the  $c$  lattice parameter is increased by  $\sim 4\%$  (at the DFT+ $U$  and DFT+ $U+V$  levels of theory). In the case of the substitutional doping (B, C, and E), all lattice parameters are increased by  $\sim 1\%$  (at the DFT+ $U$  and DFT+ $U+V$  levels of theory). In contrast, the experimental lattice parameters for the Fe-doped  $\alpha$ -MnO<sub>2</sub> are  $a_{\text{exp}} = b_{\text{exp}} = 9.83 \text{ \AA}$  and  $c_{\text{exp}} = 2.86 \text{ \AA}$ <sup>29</sup> meaning that there are no noticeable changes with respect to the pristine case (cf. Table 2).<sup>2,86,87</sup> It should be noted that the uncertainties in the experimental crystal structure parameters are relatively large, and hence more accurate experiments are needed to ascertain possible small changes in the crystal structure due to

doping.

We analyzed also the bond lengths and angles for the A and D types of doping (see Fig. S2 and Table S3 in SI). We find that due to the Fe doping some Mn–O bonds contract and some expand, and they cover a range of about 1.8 – 2.1 Å. The Fe–O bonds are symmetrical in the A type and they have different lengths in the D type (in the range 2.1 – 2.2 Å). The bond angles Mn–O–Mn are also distorted and their exact values are listed in Table S3 in SI. Finally, the O–Fe–O angles are 90° in the A type and they deviate slightly from 90° in the D type, while the Fe–O–Mn angles are in the range 123 – 126°. We are not aware of any experimental data for the bond angles and lengths in the Fe-doped  $\alpha$ -MnO<sub>2</sub>, hence the accuracy of these predictions cannot be verified at present, which motivates a strong need for new experiments.

### 3.2.3 Energetics

As in the case of the pristine  $\alpha$ -MnO<sub>2</sub> (see Sec. 3.1.3), we compare the total energies of various spin configurations in the case of the Fe-doped  $\alpha$ -MnO<sub>2</sub>. It is important to note that since the number of atoms in the simulation cell is not the same for the interstitial and substitutional doping, we can compare the total energies only for spin configurations having the same number of atoms.

As can be seen in Table 4 which is for the interstitial doping, the trends are different at different levels of theory. Namely, DFT predicts the D type to be more energetically favorable than the A type, while DFT+ $U$  predicts the opposite trend. Hence, the onsite Hubbard  $U$  correction for Mn( $3d$ ) and Fe( $3d$ ) states influences significantly the overall energetics of the system. Remarkably, when the intersite Hubbard  $V$  corrections for Mn–O and Fe–O couples are also included, the trend reverses back to the one found in DFT. This shows that intersite Hubbard interactions play a decisive role in stabilizing back the D type in the presence of localized  $3d$  electrons on Mn and Fe ions. Hence, the delicate interplay between the onsite localization and intersite hybridization due to covalent bonding is captured by DFT+ $U$ + $V$

Table 4: Total energy difference (in eV) in the case of the interstitial doping  $\text{FeMn}_8\text{O}_{16}$  (A and D). The zero of energy corresponds to the lowest-energy structure within each level of theory.

Magnetic ordering	DFT	DFT+ $U$	DFT+ $U+V$
A	0.855	0	0.254
D	0	0.072	0

Table 5: Total energy difference (in eV) in the case of the substitutional doping  $\text{FeMn}_7\text{O}_{16}$  (B, C, and E). The zero of energy corresponds to the lowest-energy structure within each level of theory.

Magnetic ordering	DFT	DFT+ $U$	DFT+ $U+V$
B	0.802	0.296	0.357
C	0.798	0.287	0.313
E	0	0	0

but not by DFT+ $U$ . Instead, in DFT apparently there is a cancellation of errors which might explain why the D type turns out to be the most energetically favorable as in DFT+ $U+V$ . Therefore, our most accurate level of theory DFT+ $U+V$  predicts that the D type is more energetically favorable than the A type. This is physically sound since the doping of  $\alpha\text{-MnO}_2$  with Fe is likely to preserve the C2-AFM character of the host; in contrast, switching from C2-AFM to the FM character due to doping would require swapping spins on half of the Mn atoms which has high energetic cost and hence it is less likely.

In the case of the substitutional doping we find that all levels of theory predict the E type to be the most energetically favorable, as can be seen in Table 5. Interestingly, for this type of doping the onsite Hubbard  $U$  correction alone is able to capture the right energetics of the system at variance with the case of the interstitial doping. Thus, again we find that doping of  $\alpha\text{-MnO}_2$  with Fe preserves the C2-AFM character of the host when making a partial substitution of Mn for Fe.

In order to gain more insights about the chemistry of the Fe-doped  $\alpha\text{-MnO}_2$  it would be instructive to compute and compare the defect formation energies for different magnetic orderings shown in Fig. 7.<sup>98,99</sup> This would require carrying out a careful and thorough analysis

of calculations using supercells and different charge states of Fe. However, this goes beyond the scope of the current work and will be investigated in the forthcoming study.

In the following we focus mainly on the D and E type magnetic orderings since these are the lowest-energy configurations within DFT+ $U$ + $V$ .

### 3.2.4 Magnetic moment

The magnetic moments on Mn and Fe atoms for the Fe-doped  $\alpha$ -MnO<sub>2</sub> computed at different levels of theory for the D and E types are shown in Fig. 8 (see Fig. S3 in SI for the magnetic moments for the A, B, and C types). We are not aware of any experimental reports of magnetic moments for the Fe-doped  $\alpha$ -MnO<sub>2</sub>, hence we present the analysis based on a comparison with the magnetic moments in the pristine  $\alpha$ -MnO<sub>2</sub> (see Sec. 3.1.4).

By comparing Figs. 4 and 8 we can see that there are no big changes in the magnetic moments on Mn atoms after the Fe doping. Moreover, we still see the same trends as in the case of the pristine  $\alpha$ -MnO<sub>2</sub>: DFT and DFT+ $U$  give the smallest and the largest magnetic moments, respectively, while DFT+ $U$ + $V$  gives magnetic moments that are only slightly smaller (by  $\sim 0.2\mu_B$ ) than those obtained from DFT+ $U$ .

The magnetic moments on Fe atoms are very similar within DFT+ $U$  and DFT+ $U$ + $V$  (especially for the D type), in contrast to the magnetic moments on Mn atoms which have larger differences between DFT+ $U$  and DFT+ $U$ + $V$ . This is due to the fact that Mn atoms have stronger covalent bonding with ligands,<sup>53</sup> and hence the magnetic moments are affected stronger by the intersite Hubbard  $V$  corrections. Within DFT, the values of magnetic moments on Fe atoms are scattered (for different spin configurations) much more than in the case of DFT+ $U$  and DFT+ $U$ + $V$ . This is due to the failure of DFT with standard functionals (LSDA and  $\sigma$ -GGA) to describe accurately the electronic and magnetic properties of Fe due to large self-interaction errors for  $3d$  electrons. Interestingly, the scattering of magnetic moments on Mn atoms in the case of DFT is much smaller than for Fe. Finally, it would be desirable to have the experimental data for the magnetic moments on Mn and Fe in the



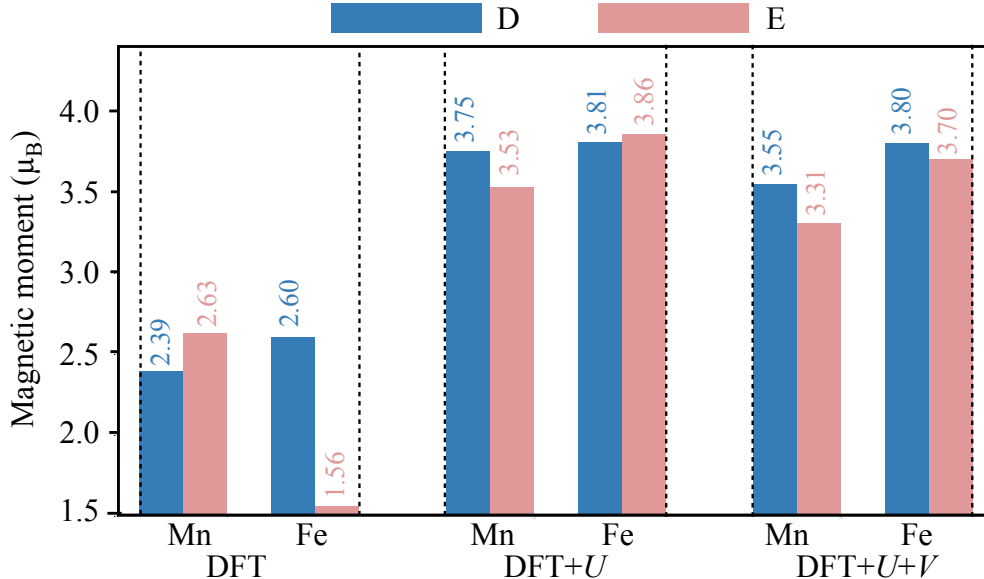


Figure 8: Magnetic moment (in  $\mu_B$ ) on Mn and Fe atoms in the Fe-doped  $\alpha$ -MnO<sub>2</sub> for two collinear magnetic orderings (D and E types) computed at three levels of theory (DFT, DFT+ $U$ , and DFT+ $U$ + $V$ ) using the PBEsol functional. For each case, the Hubbard parameters  $U$  and  $V$  were computed using DFPT and are listed in Table 3.

Fe-doped  $\alpha$ -MnO<sub>2</sub> which would allow us to check the accuracy of computational predictions of this work.

### 3.2.5 Projected density of states

After the Fe doping of  $\alpha$ -MnO<sub>2</sub> the electronic structure of this material changes significantly as can be seen in Figs. 9 (a) and (b) that show the spin-resolved PDOS and total DOS computed using DFT+ $U$  and DFT+ $U$ + $V$  for the D and E types of doping (see Fig. S4 in SI for the PDOS for the A, B, and C types). We note in passing that the PDOS of the Fe-doped  $\alpha$ -MnO<sub>2</sub> computed using DFT is unreliable [like in the case of the pristine  $\alpha$ -MnO<sub>2</sub>, see Fig. 6 (a)] due to the overdelocalization of  $3d$  electrons of Mn and Fe atoms (see Fig. S5 in SI). As can be seen in Fig. 9, the doped material turns out to be a metal in the case of the D type doping, while the E type shows a semiconducting behavior with a small band gap of 0.21 eV in the case of DFT+ $U$  and 0.56 eV in the case of DFT+ $U$ + $V$ . From the experimental side, we are aware of Ref.<sup>100</sup> that reports a band gap of 0.30 eV at

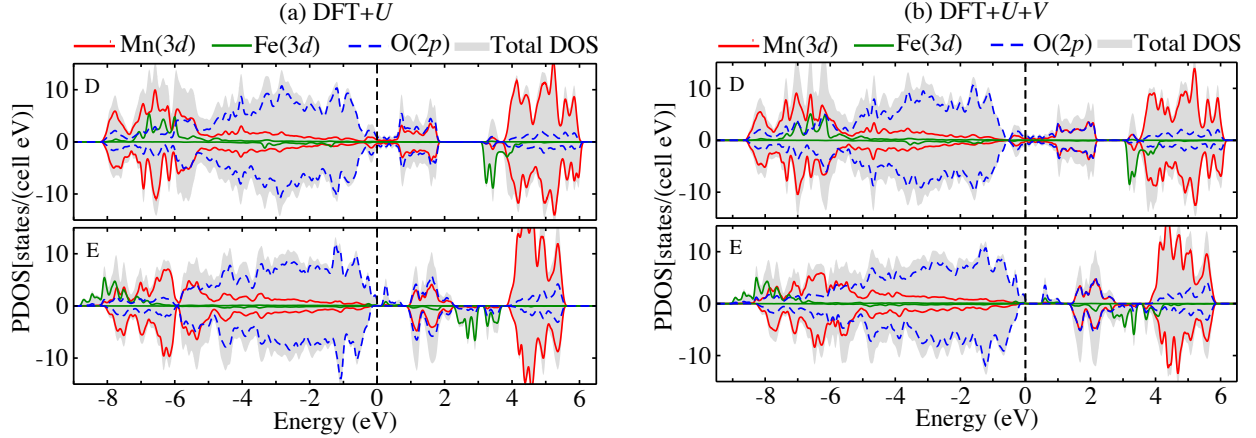


Figure 9: Spin-resolved PDOS and total DOS for two collinear magnetic orderings of the Fe-doped  $\alpha$ -MnO<sub>2</sub> (D and E) computed using the PBEsol functional within (a) DFT+ $U$ , and (b) DFT+ $U$ + $V$ . For each case the Hubbard parameters  $U$  and  $V$  were computed using DFPT and are listed in Table 3. Upper panels correspond to the spin-up components, while lower panels correspond to the spin-down components. The zero of energy corresponds to the Fermi energy (in the case of metallic ground states) or top of the valence bands (in the case of insulating ground states).

low Fe concentrations (5 mol%). It is important to note, though, that a significant amount of water was accumulated in the tunnels of the Fe-doped  $\alpha$ -MnO<sub>2</sub> samples in Ref. <sup>100</sup> hence the band gap value reported above might not be very reliable. Nonetheless, both DFT+ $U$  and DFT+ $U$ + $V$  predict a band gap for the E type which is qualitatively consistent with the finding of Ref. <sup>100</sup> In contrast, for the D type we do not find a band gap, though the DOS at the Fermi level is extremely small (see also Fig. S6 in SI). Therefore, since it is not known which type of doping is dominant in the samples of Ref. <sup>100</sup> (interstitial or substitutional), our DFT+ $U$ + $V$  calculations for the two best candidates (D and E types) can be considered as satisfactory. Obviously, more experiments on the accurate band gap determination in the Fe-doped  $\alpha$ -MnO<sub>2</sub> are needed.

Of particular interest is to analyze the position of the Fe(3d) states in the spin-resolved PDOS of the Fe-doped  $\alpha$ -MnO<sub>2</sub>. As can be seen in Fig. 9, in the case of the interstitial doping (D type) these states appear around  $-6.5$  eV and  $3.5$  eV in the spin-up and spin-down channels, respectively, while in the case of the substitutional doping (E type) they appear around  $-8.0$  eV and  $2.8$  eV in the spin-up and spin-down channels, respectively. This

information could be useful when interpreting the XPS and XANES spectra to determine which type of doping is present in the samples. DFT+ $U$  and DFT+ $U+V$  predict similar position and shape of the peaks due to Fe( $3d$ ) states in the PDOS; the main differences are mainly around the Fermi level (for the A, B, C, and D types) or top of the valence bands (for the E type). Finally, we note that the empty Fe( $3d$ ) states in the spin-down channel have negligible hybridization with the O( $2p$ ) states, while in the spin-up channel the hybridization of the occupied Fe( $3d$ ) states with the O( $2p$ ) states is not very strong. Thus, the intersite  $V$  correction for the Fe–O couples is likely not crucial when describing the relative position of the Fe( $3d$ ) and O( $2p$ ) states, while it is relevant for the Mn–O couples which show stronger hybridization especially for the lowest conduction bands.

### 3.2.6 Oxidation state

The OS of Mn and Fe in the Fe-doped  $\alpha$ -MnO<sub>2</sub> is actively discussed in the experimental literature.<sup>24,27–30</sup> In Refs. <sup>24,27,29,30</sup> it is reported that there is a mixture of two types of Mn with the OS of +4 and +3. It is argued that Mn<sup>3+</sup> is present due to the appearance of the oxygen vacancies after the Fe doping. The OS of Fe is also reported to be +4 and +3, with Fe<sup>4+</sup> being present also due to the oxygen vacancies,<sup>29</sup> while in Ref. <sup>28</sup> it is argued that the OS of Fe is exclusively +3. Computational studies could be useful to verify these experimental findings and assumptions.

In this work we do not consider oxygen vacancies in the Fe-doped  $\alpha$ -MnO<sub>2</sub> because, first of all, we seek to understand what are the differences in the OS of Mn and Fe for different types of doping (interstitial and substitutional) in the idealized case. We stress that here we consider only neutral Fe dopants. The determination of OS is not a trivial task.<sup>101–103</sup> In particular, using the Löwdin occupations as a proxy for determining the OS could often be misleading.<sup>20,102</sup> Here we use the projection-based method of Ref. <sup>66</sup> that has proven to be effective for determining the OS of transition-metal elements in various complex materials.<sup>20,104</sup> The main idea is based on the count of the eigenvalues of the site-diagonal

occupation matrix [see Eq. (S3) in SI] that are close to unity. Using this approach and our DFT+ $U+V$  data for the C2-AFM pristine  $\alpha$ -MnO<sub>2</sub> we find that the OS of Mn is +4, which agrees with the nominal OS. In Table S4 in SI we report the eigenvalues of the site-diagonal occupation matrix for the D and E types of the Fe-doped  $\alpha$ -MnO<sub>2</sub>. We find that in both cases the OS of Mn is +4, while the OS of Fe is +2 in the D type and +4 in the E type. These findings are physically sound and could be interpreted as follows. In the D type doping, where dopant ions reside in the  $2 \times 2$  tunnels, there is a charge transfer from the 4s shell of Fe towards four nearest-neighbor O atoms (see Fig. S2 in SI), while the 3d shell of Fe remains intact (thus Fe is in a high-spin state,  $d^5(\uparrow)d^1(\downarrow)$ ). We note though that the 4s shell of Fe is not fully empty because the 2 electrons from this shell are actually shared with the nearest four oxygens via hybridizations between the Fe-4s and O-2p orbitals. In contrast, in the E type doping, where the dopant ions partially substitute Mn atoms, Fe tries to adapt itself to the local chemical environment and hence it has the same OS as Mn, i.e. +4. As a consequence, in this case Fe “loses” 2 electrons from the 4s shell and 2 electrons from the 3d shell, and thus only 4 electrons remain in the 3d shell in the high-spin state,  $d^4(\uparrow)d^0(\downarrow)$ . The charge transfer occurs from Fe to six O atoms within the FeO<sub>6</sub> octahedron. To be more precise, Fe does not lose *fully* these 4 electrons, but it shares them with O atoms by creating covalent bonds, and as a consequence there are fractional atomic occupations of those levels (i.e. the eigenvalues of the occupation matrix have fractional values between 0 and 1).<sup>66</sup> Obviously, the chemistry of the Fe-doped  $\alpha$ -MnO<sub>2</sub> will change in the case when there are oxygen vacancies (see e.g. Ref.<sup>30</sup>) and this will be the topic of future investigations.

## 4 Conclusions

We have presented a first-principles study of the structural, electronic, and magnetic properties of the pristine and Fe-doped  $\alpha$ -MnO<sub>2</sub> using DFT with extended Hubbard functionals. The onsite and intersite Hubbard parameters were computed self-consistently using DFPT

in the basis of Löwdin-orthogonalized atomic orbitals. We found that DFT+ $U$  provides quite accurate description of the ground-state properties of the pristine  $\alpha$ -MnO<sub>2</sub>, while the intersite Hubbard  $V$  corrections are not decisive though they lead to important quantitative improvements. In particular, we found that the C2-AFM spin configuration is the most energetically favorable one (compared to the FM and other types of the AFM magnetic orderings) in the pristine  $\alpha$ -MnO<sub>2</sub>, both within DFT+ $U$  and DFT+ $U+V$ . This finding shows the superiority of DFT+ $U$  and DFT+ $U+V$  (with  $U$  and  $V$  determined from linear-response theory) compared to HSE06: the latter fails to predict the antiferromagnetic ground state to be lower in energy than FM and thus contradicts to experiments.<sup>41</sup> Overall, the computed crystal structure properties and the band gap of the pristine  $\alpha$ -MnO<sub>2</sub> are in good agreement with experiments, both within DFT+ $U$  and DFT+ $U+V$ , while the magnetic moments are somewhat underestimated.

In contrast, in the Fe-doped  $\alpha$ -MnO<sub>2</sub> the onsite Hubbard  $U$  corrections alone are unable to predict the correct trends for the interstitial doping and the intersite Hubbard  $V$  corrections are crucial. Namely, we find that the interstitial doping preserves the C2-AFM spin configuration of the host lattice only when both onsite  $U$  and intersite  $V$  Hubbard corrections are included, while for the substitutional doping the onsite Hubbard  $U$  correction alone is able to preserve the C2-AFM spin configuration of the host lattice. In addition, the oxidation state of Fe in the two types of doping is found to be different: it is +2 in the case of the interstitial doping, and +4 in the case of the substitutional doping. The oxidation state of Mn is +4 in the pristine and all types of the Fe-doped  $\alpha$ -MnO<sub>2</sub>. Finally, we found that the semiconducting character of  $\alpha$ -MnO<sub>2</sub> is preserved in the case of the substitutional doping (E type), while the material becomes metallic with a vanishing DOS at the Fermi level in the case of the interstitial doping (D type).

Finally, this work paves the way for future studies of  $\alpha$ -MnO<sub>2</sub> doped not only with Fe but also other transitional-metal elements or cations in the presence of oxygen vacancies or under strain, as well as the calculation of the defect formation energies.<sup>98,99</sup>

## Supporting Information Available

Description of the computational method, crystal structure properties, projected density of states, and the population analysis.

## Acknowledgement

We thank Sokseiha Muy, Nicola Seriani, Ralph Gebauer, and Ankita Mathur for fruitful discussions. R.M. acknowledges support by the IIT Mandi for the HTRA fellowship. I.T. acknowledges support by the NCCR MARVEL, a National Centre of Competence in Research, funded by the Swiss National Science Foundation (Grant number 182892). Computer time was provided by the Holland Computing Centre (University of Nebraska) and by the Swiss National Supercomputing Centre (CSCS) under project No. s1073.

## References

- (1) Ghosh, S. Diversity in the Family of Manganese Oxides at the Nanoscale: from Fundamentals to Applications. *ACS Omega* **2020**, *5*, 25493.
- (2) Thackeray, M. M. Manganese Oxides for Lithium Batteries. *Prog. Solid. State Ch.* **1997**, *25*, 1–71.
- (3) Barudžija, T.; Kusigerski, V.; Cvjetičanin, N.; Šorgić, S.; Perović, M.; Mitrić, M. Structural and Magnetic Properties of Hydrothermally Synthesized  $\beta$ -MnO<sub>2</sub> and  $\alpha$ -K<sub>X</sub>MnO<sub>2</sub> Nanorods. *J. Alloys Compd.* **2016**, *665*, 261–270.
- (4) Brady, A. B.; Tallman, K. R.; Takeuchi, E. S.; Marschilok, A. C.; Takeuchi, K. J.; Liu, P. Transition Metal Substitution of Hollandite  $\alpha$ -MnO<sub>2</sub>: Enhanced Potential and Structural Stability on Lithiation from First-Principles Calculation. *J. Phys. Chem. C* **2019**, *123*, 25042–25051.

- (5) Lübke, M.; Sumboja, A.; McCafferty, L.; Armer, C. F.; Handoko, A. D.; Du, Y.; McColl, K.; Cora, F.; Brett, D.; Liu, Z., et al. Transition-Metal-Doped  $\alpha$ -MnO<sub>2</sub> Nanorods as Bifunctional Catalysts for Efficient Oxygen Reduction and Evolution Reactions. *ChemistrySelect* **2018**, *3*, 2613–2622.
- (6) Hashem, A.; Abuzeid, H.; Mikhailova, D.; Ehrenberg, H.; Mauger, A.; Julien, C. Structural and Electrochemical Properties of  $\alpha$ -MnO<sub>2</sub> Doped with Cobalt. *J. Mater. Sci.* **2012**, *47*, 2479–2485.
- (7) Xu, S.; Li, S.-P.; Wang, T.; Wang, C.-F. Effect of Surface Ionization of Doped MnO<sub>2</sub> on Capacitive Deionization Efficiency. *Langmuir* **2019**, *35*, 628–640.
- (8) Song, Z.; Yan, Z.; Yang, X.; Bai, H.; Duan, Y.; Yang, B.; Leng, L. First Principles Density Functional Theory Study of Pb Doped  $\alpha$ -MnO<sub>2</sub> Catalytic Materials. *Chem. Phys. Lett.* **2018**, *695*, 216–221.
- (9) Li, T.; Wu, J.; Xiao, X.; Zhang, B.; Hu, Z.; Zhou, J.; Yang, P.; Chen, X.; Wang, B.; Huang, L. Band Gap Engineering of MnO<sub>2</sub> Through in Situ Al-Doping for Applicable Pseudocapacitors. *RSC advances* **2016**, *6*, 13914–13919.
- (10) Ochoa, F. S.; Huang, Z.; Tang, X.; Coccoletzi, G. H.; Springborg, M. Magnetostructural Phase Transition Assisted by Temperature in Ag- $\alpha$ MnO<sub>2</sub>: A Density Functional Theory Study. *Phys. Chem. Chem. Phys.* **2016**, *18*, 7442–7448.
- (11) Chen, K.; Pan, W.; Xue, D. Phase Transformation of Ce<sup>3+</sup>-Doped MnO<sub>2</sub> for Pseudocapacitive Electrode Materials. *J. Phys. Chem. C* **2016**, *120*, 20077–20081.
- (12) Zhang, R.; Yu, X.; Nam, K.-W.; Ling, C.; Arthur, T. S.; Song, W.; Knapp, A. M.; Ehrlich, S. N.; Yang, X.-Q.; Matsui, M.  $\alpha$ -MnO<sub>2</sub> as a Cathode Material for Rechargeable Mg Batteries. *Electrochem. commun.* **2012**, *23*, 110–113.

- (13) Débart, A.; Paterson, A. J.; Bao, J.; Bruce, P. G.  $\alpha$ -MnO<sub>2</sub> Nanowires: A catalyst for the O<sub>2</sub> Electrode in Rechargeable Lithium Batteries. *Angew. Chem. Int. Ed.* **2008**, *47*, 4521–4524.
- (14) Tompsett, D. A.; Islam, M. S. Electrochemistry of Hollandite  $\alpha$ -MnO<sub>2</sub>: Li-Ion and Na-Ion Insertion and Li<sub>2</sub>O Incorporation. *Chem. Mater.* **2013**, *25*, 2515–2526.
- (15) Wu, Z.-S.; Ren, W.; Wang, D.-W.; Li, F.; Liu, B.; Cheng, H.-M. High-Energy MnO<sub>2</sub> Nanowire/Graphene and Graphene Asymmetric Electrochemical Capacitors. *ACS nano* **2010**, *4*, 5835–5842.
- (16) Kruthika, G.; Karthikeyan, J.; Murugan, P. Tuning of Intrinsic Antiferromagnetic to Ferromagnetic Ordering in Microporous  $\alpha$ -MnO<sub>2</sub> by Inducing Tensile Strain. *Phys. Chem. Chem. Phys.* **2017**, *19*, 3770–3776.
- (17) Boppana, V. B. R.; Jiao, F. Nanostructured MnO<sub>2</sub>: An Efficient and Robust Water Oxidation Catalyst. *ChemComm* **2011**, *47*, 8973–8975.
- (18) Liang, S.; Teng, F.; Bulgan, G.; Zong, R.; Zhu, Y. Effect of Phase Structure of MnO<sub>2</sub> Nanorod Catalyst on the Activity for CO Oxidation. *J. Phys. Chem. C* **2008**, *112*, 5307–5315.
- (19) Liu, W.-X.; Zhu, X.-L.; Liu, S.-Q.; Gu, Q.-Q.; Meng, Z.-D. Near-Infrared-Driven Selective Photocatalytic Removal of Ammonia based on Valence Band Recognition of an  $\alpha$ -MnO<sub>2</sub>/N-Doped Graphene Hybrid Catalyst. *ACS omega* **2018**, *3*, 5537–5546.
- (20) Yamamoto, N.; Endo, T.; Shimada, M.; Takada, T. Single Crystal Growth of  $\alpha$ -MnO<sub>2</sub>. *Jpn. J. Appl. Phys.* **1974**, *13*, 723–724.
- (21) Zhao, J.; Yin, J.; Yang, S. Hydrothermal Synthesis and Magnetic Properties of  $\alpha$ -MnO<sub>2</sub> Nanowires. *Mater. Res. Bull.* **2012**, *47*, 896–900.



- (22) Kumar, A.; Sanger, A.; Singh, A. K.; Kumar, A.; Kumar, M.; Chandra, R. Experimental Evidence of Spin Glass and Exchange Bias Behavior in Sputtered Grown  $\alpha$ -MnO<sub>2</sub> Nanorods. *J. Magn. Magn. Mater.* **2017**, *433*, 227–233.
- (23) Zhou, C.; Wang, J.; Liu, X.; Chen, F.; Di, Y.; Gao, S.; Shi, Q. Magnetic and Thermodynamic Properties of  $\alpha$ ,  $\beta$ ,  $\gamma$  and  $\delta$ -MnO<sub>2</sub>. *New J. Chem.* **2018**, *42*, 8400.
- (24) Hui, J.; Yuping, D.; Zhuo, L.; Jia, Z.; Shunhua, L. Influence of Fe-Doping on the Microstructure and Electromagnetic Performance of Manganese Oxides. *Physica B: Condensed Matter* **2012**, *407*, 971.
- (25) Said, S.; El Maghrabi, H. H.; Riad, M.; Mikhail, S. Photo-Catalytic Selective Organic Transformations by Fe-Doped Octahedral Molecular Sieves (Manganese Oxide) Nano-Structure. *J. Asian Ceram. Soc.* **2018**, *6*, 169–181.
- (26) Mathur, A.; Halder, A. One-Step Synthesis of Bifunctional Iron-Doped Manganese Oxide Nanorods for Rechargeable Zinc–Air Batteries. *Catal. Sci. Technol.* **2019**, *9*, 1245–1254.
- (27) Duan, Y.; Jing, H.; Liu, Z.; Li, S.; Ma, G. Controlled Synthesis and Electromagnetic Performance of Hollow Microstructures Assembled of Tetragonal MnO<sub>2</sub> Nano-Columns. *J. Appl. Phys.* **2012**, *111*, 084109.
- (28) Li, Z.; Gu, A.; Lou, Z.; Sun, J.; Zhou, Q.; Chan, K. Y. Facile Synthesis of Iron-Doped Hollow Urchin-like MnO<sub>2</sub> for Supercapacitors. *J. Mater. Sci.* **2017**, *52*, 4852–4865.
- (29) Song, L.; Duan, Y.; Cui, Y.; Huang, Z. Fe-Doped MnO<sub>2</sub> Nanostructures for Attenuation–Impedance Balance-Boosted Microwave Absorption. *ACS Appl. Nano Mater.* **2022**, *5*, 2738.
- (30) Fan, C.; Li, K.; Peng, Y.; Duan, R.; Hu, F.; Jing, Q.; Chen, J.; Li, J. Fe-Doped  $\alpha$ -MnO<sub>2</sub> Nanorods for the Catalytic Removal of NO<sub>x</sub> and Chlorobenzene: the Relationship

- between Lattice Distortion and Catalytic Redox Properties. *Phys. Chem. Chem. Phys.* **2019**, *21*, 25880–25888.
- (31) Duan, Y.; Liu, Z.; Zhang, Y.; Wen, M. A Theoretical Study of the Dielectric and Magnetic Responses of Fe-Doped  $\alpha$ -MnO<sub>2</sub> Based on Quantum Mechanical Calculations. *J. Mater. Chem. C* **2013**, *1*, 1990–1994.
- (32) Momma, K.; Izumi, F. VESTA: A Three-dimensional Visualization System for Electronic and Structural Analysis. *J. Appl. Crystallogr.* **2008**, *41*, 653.
- (33) Hohenberg, P.; Kohn, W. Inhomogeneous Electron Gas. *Phys. Rev.* **1964**, *136*, B864.
- (34) Kohn, W.; Sham, L. Self-Consistent Equations Including Exchange and Correlation Effects. *Phys. Rev.* **1965**, *140*, A1133.
- (35) Perdew, J.; Zunger, A. Self-Interaction Correction to Density-Functional Approximations for Many-Electron Systems. *Phys. Rev. B* **1981**, *23*, 5048.
- (36) Mori-Sánchez, P.; Cohen, A. J.; Yang, W. Many-Electron Self-Interaction Error in Approximate Density Functionals. *J. Chem. Phys.* **2006**, *125*, 201102.
- (37) Anisimov, V. I.; Zaanen, J.; Andersen, O. K. Band Theory and Mott Insulators: Hubbard  $U$  Instead of Stoner  $I$ . *Phys. Rev. B* **1991**, *44*, 943.
- (38) Liechtenstein, A.; Anisimov, V. I.; Zaanen, J. Density-Functional Theory and Strong Interactions: Orbital Ordering in Mott-Hubbard Insulators. *Phys. Rev. B* **1995**, *52*, R5467.
- (39) Dudarev, S.; Botton, G.; Savrasov, S.; Humphreys, C.; Sutton, A. Electron-Energy-Loss Spectra and the Structural Stability of Nickel Oxide: An LSDA+ $U$  Study. *Phys. Rev. B* **1998**, *57*, 1505.
- (40) Cockayne, E.; Li, L. First-principles DFT+ $U$  Studies of the Atomic, Electronic, and Magnetic Structure of  $\alpha$ -MnO<sub>2</sub> (Cryptomelane). *Chem. Phys. Lett.* **2012**, *544*, 53–58.

- (41) Crespo, Y.; Seriani, N. Electronic and Magnetic Properties of  $\alpha$ -MnO<sub>2</sub> from Ab Initio Calculations. *Phys. Rev. B* **2013**, *88*, 144428.
- (42) Kitchaev, D. A.; Peng, H.; Liu, Y.; Sun, J.; Perdew, J. P.; Ceder, G. Energetics of MnO<sub>2</sub> Polymorphs in Density Functional Theory. *Phys. Rev. B* **2016**, *93*, 045132.
- (43) Chepkoech, M.; Joubert, D. P.; Amolo, G. O. First Principles Calculations of the Thermoelectric Properties of  $\alpha$ -MnO<sub>2</sub> and  $\beta$ -MnO<sub>2</sub>. *Eur Phys J B* **2018**, *91*, 1–11.
- (44) Heyd, J.; Scuseria, G.; Ernzerhof, M. Hybrid Functionals based on a Screened Coulomb Potential. *J. Chem. Phys.* **2003**, *118*, 8207.
- (45) Heyd, J.; Scuseria, G.; Ernzerhof, M. Erratum: “Hybrid Functionals Based on a Screened Coulomb Potential”. *J. Chem. Phys.* **2006**, *124*, 219906.
- (46) Noda, Y.; Ohno, K.; Nakamura, S. Momentum-Dependent Band Spin Splitting in Semiconducting MnO<sub>2</sub>: A Density Functional Calculation. *Phys. Chem. Chem. Phys.* **2016**, *18*, 13294–13303.
- (47) Kaltak, M.; Fernandez-Serra, M.; Hybertsen, M. S. Charge Localization and Ordering in A<sub>2</sub>Mn<sub>8</sub>O<sub>16</sub> Hollandite Group Oxides: Impact of Density Functional Theory Approaches. *Phys. Rev. Mater.* **2017**, *1*, 075401.
- (48) Wang, Y.-C.; Chen, Z.-H.; Jiang, H. The Local Projection in the Density Functional Theory Plus  $U$  Approach: A Critical Assessment. *J. Chem. Phys.* **2016**, *144*, 144106.
- (49) Kulik, H.; Marzari, N. A Self-Consistent Hubbard  $U$  Density-Functional Theory Approach to the Addition-Elimination Reactions of Hydrocarbons on Bare FeO<sup>+</sup>. *J. Chem. Phys.* **2008**, *129*, 134314.
- (50) Mahajan, R.; Timrov, I.; Marzari, N.; Kashyap, A. Importance of Intersite Hubbard Interactions in  $\beta$ -MnO<sub>2</sub>: A First-Principles DFT+ $U$ + $V$  Study. *Phys. Rev. Materials* **2021**, *5*, 104402.

- (51) Campo Jr, V. L.; Cococcioni, M. Extended DFT+ $U$ + $V$  Method with On-site and Inter-site Electronic Interactions. *J. Phys. Condens. Matter* **2010**, *22*, 055602.
- (52) Kulik, H.; Marzari, N. Transition-Metal Dioxides: A Case for the Intersite Term in Hubbard-Model Functionals. *J. Chem. Phys.* **2011**, *134*, 094103.
- (53) Cococcioni, M.; Marzari, N. Energetics and Cathode Voltages of LiMPO<sub>4</sub> Olivines (M= Fe, Mn) from Extended Hubbard Functionals. *Phys. Rev. Materials* **2019**, *3*, 033801.
- (54) Ricca, C.; Timrov, I.; Cococcioni, M.; Marzari, N.; Aschauer, U. Self-Consistent DFT+ $U$ + $V$  Study of Oxygen Vacancies in SrTiO<sub>3</sub>. *Phys. Rev. Research* **2020**, *2*, 023313.
- (55) Timrov, I.; Agrawal, P.; Zhang, X.; Erat, S.; Liu, R.; Braun, A.; Cococcioni, M.; Calandra, M.; Marzari, N.; Passerone, D. Electronic Structure of Ni-Substituted LaFeO<sub>3</sub> from Near Edge X-ray Absorption Fine Structure Experiments and First-Principles Simulations. *Phys. Rev. Research* **2020**, *2*, 033265.
- (56) Cococcioni, M.; Floris, A. Magnetic Energy Landscape of Dimolybdenum Tetraacetate on a Bulk Insulator Surface. *Appl. Sci.* **2021**, *11*, 3806.
- (57) Yang, W.; Jhi, S.-H.; Lee, S.-H.; Son, Y.-W. *Ab initio* Study of Lattice Dynamics of Group IV Semiconductors using Pseudohybrid Functionals for Extended Hubbard Interactions. *Phys. Rev. B* **2021**, *104*, 104313.
- (58) Jang, B.; Kim, M.; Lee, S.-H.; Yang, W.; Jhi, S.-H.; Son, Y.-W. Decisive Roles of Intersite Coulomb Interactions in Charge Ordered Systems. Cornell University, <https://arxiv.org/abs/2205.02470> (submitted May 5, 2022; accessed July 28, 2022).
- (59) Yang, W.; Jang, B.; Son, Y.-W.; Jhi, S.-H. Lattice Dynamical Properties of Antiferromagnetic Oxides Calculated using Self-consistent Extended Hubbard Functional Method. *J. Phys.: Condens. Matter* **2022**, *34*, 295601.

- (20) Timrov, I.; Aquilante, F.; Cococcioni, M.; Marzari, N. Accurate Electronic Properties and Intercalation Voltages of Olivine-type Li-ion Cathode Materials from Extended Hubbard Functionals. Cornell University, <https://arxiv.org/abs/2203.15732> (submitted March 29, 2022; accessed July 28, 2022).
- (61) Timrov, I.; Marzari, N.; Cococcioni, M. Hubbard Parameters from Density-Functional Perturbation Theory. *Phys. Rev. B* **2018**, *98*, 085127.
- (62) Timrov, I.; Marzari, N.; Cococcioni, M. Self-Consistent Hubbard Parameters from Density-Functional Perturbation Theory in the Ultrasoft and Projector-Augmented Wave Formulations. *Phys. Rev. B* **2021**, *103*, 045141.
- (63) Hsu, H.; Umemoto, K.; Cococcioni, M.; Wentzcovitch, R. First-Principles Study for Low-Spin  $\text{LaCoO}_3$  with a Structurally Consistent Hubbard  $U$ . *Phys. Rev. B* **2009**, *79*, 125124.
- (64) Goodenough, J. B. Theory of the Role of Covalence in the Perovskite-Type Manganites [La, M (II)]  $\text{MnO}_3$ . *Phys. Rev.* **1955**, *100*, 564.
- (65) Kanamori, J. Superexchange Interaction and Symmetry Properties of Electron Orbitals. *J. Phys. Chem. Solid.* **1959**, *10*, 87–98.
- (66) Sit, P. H.-L.; Car, R.; Cohen, M. H.; Selloni, A. Simple, Unambiguous Theoretical Approach to Oxidation State Determination via First-Principles Calculations. *Inorg. Chem.* **2011**, *50*, 10259.
- (67) Giannozzi, P.; Baroni, S.; Bonini, N.; Calandra, M.; Car, R.; Cavazzoni, C.; Ceresoli, D.; Chiarotti, G.; Cococcioni, M.; Dabo, I., et al. Quantum ESPRESSO: A Modular and Open-Source Software Project for Quantum Simulations of Materials. *J. Phys.: Condens. Matter.* **2009**, *21*, 395502.

- (68) Giannozzi, P.; Andreussi, O.; Brumme, T.; Bunau, O.; Buongiorno Nardelli, M.; Calandra, M.; Car, R.; Cavazzoni, C.; Ceresoli, D.; Cococcioni, M., et al. Advanced Capabilities for Materials Modelling with Quantum ESPRESSO. *J. Phys.: Condens. Matter.* **2017**, *29*, 465901.
- (69) Giannozzi, P.; Baseggio, O.; Bonfà, P.; Brunato, D.; Car, R.; Carnimeo, I.; Cavazzoni, C.; de Gironcoli, S.; Delugas, P.; Ferrari Ruffino, F., et al. Quantum ESPRESSO Toward the Exascale. *J. Chem. Phys.* **2020**, *152*, 154105.
- (70) Perdew, J. P.; Ruzsinszky, A.; Csonka, G. I.; Vydrov, O. A.; Scuseria, G. E.; Constantin, L. A.; Zhou, X.; Burke, K. Restoring the Density-Gradient Expansion for Exchange in Solids and Surfaces. *Phys. Rev. Lett.* **2008**, *100*, 136406.
- (71) Prandini, G.; Marrazzo, A.; Castelli, I. E.; Mounet, N.; Marzari, N. Precision and Efficiency in Solid-State Pseudopotential Calculations. *npj Comput. Mater.* **2018**, *4*, 1–13.
- (72) The SSSP library of the Materials Cloud: <https://www.materialscloud.org/discover/sssp/table/precision> (accessed July 28, 2022).
- (73) Garrity, K. F.; Bennett, J. W.; Rabe, K. M.; Vanderbilt, D. Pseudopotentials for High-Throughput DFT Calculations. *Comput. Mater. Sci.* **2014**, *81*, 446–452.
- (74) Küçükbenli, E.; Monni, M.; Adetunji, B.; Ge, X.; Adebayo, G.; Marzari, N.; de Gironcoli, S.; Dal Corso, A. Projector Augmented-Wave and All-electron Calculations Across the Periodic Table: A Comparison of Structural and Energetic Properties. Cornell University, <https://arxiv.org/abs/1404.3015> (submitted April 11, 2014; accessed July 28, 2022).
- (75) Marzari, N.; Vanderbilt, D.; De Vita, A.; Payne, M. Thermal Contraction and Disorder of the Al (110) Surface. *Phys. Rev. Lett.* **1999**, *82*, 3296.

- (76) Fletcher, R. *Practical Methods of Optimization*, 2nd ed.; Wiley: Chichester, 1987.
- (77) Löwdin, P.-O. On the Non-orthogonality Problem Connected with the use of Atomic Wave Functions in the Theory of Molecules and Crystals. *J. Chem. Phys.* **1950**, *18*, 365–375.
- (78) Mayer, I. On Löwdin’s Method of Symmetric Orthogonalization. *Int. J. Quant. Chem.* **2002**, *90*, 63–65.
- (79) Timrov, I.; Aquilante, F.; Binci, L.; Cococcioni, M.; Marzari, N. Pulay Forces in Density-Functional Theory with Extended Hubbard Functionals: from Nonorthogonalized to Orthogonalized Manifolds. *Phys. Rev. B* **2020**, *102*, 235159.
- (80) Timrov, I.; Aquilante, F.; Binci, L.; Cococcioni, M.; Marzari, N. Erratum: Pulay Forces in Density-Functional Theory with Extended Hubbard Functionals: from Nonorthogonalized to Orthogonalized Manifolds. *Phys. Rev. B* **2022**, *105*, 199901(E).
- (81) Timrov, I.; Marzari, N.; Cococcioni, M. HP – A Code for the Calculation of Hubbard Parameters using Density-Functional Perturbation Theory. *Comput. Phys. Commun.* **2022**, *279*, 108455.
- (82) Mahajan, R.; Kashyap, A.; Timrov, I. Pivotal role of intersite Hubbard interactions in Fe-doped  $\alpha$ -MnO<sub>2</sub>. Materials Cloud Archive **2022.83** (2022), doi: 10.24435/materialscloud:8n-bm, <https://archive.materialscloud.org/record/2022.83> (accessed July 28, 2022).
- (83) Nawa, K.; Akiyama, T.; Ito, T.; Nakamura, K.; Oguchi, T.; Weinert, M. Scaled Effective On-site Coulomb Interaction in the DFT+*U* Method for Correlated Materials. *Phys. Rev. B* **2018**, *97*, 035117.
- (84) Kick, M.; Reuter, K.; Oberhofer, H. Intricacies of DFT+*U*, Not Only in a Numeric Atom Centered Orbital Framework. *J. Chem. Theor. Comput.* **2019**, *15*, 1705–1718.

- (85) Kirchner-Hall, N. E.; Zhao, W.; Xiong, Y.; Timrov, I.; Dabo, I. Extensive Benchmarking of DFT+*U* Calculations for Predicting Band Gaps. *Appl. Sci.* **2021**, *11*, 2395.
- (86) Islam, S.; Alfaruqi, M. H.; Song, J.; Kim, S.; Pham, D. T.; Jo, J.; Kim, S.; Mathew, V.; Baboo, J. P.; Xiu, Z., et al. Carbon-Coated Manganese Dioxide Nanoparticles and Their Enhanced Electrochemical Properties for Zinc-Ion Battery Applications. *J. Energy Chem.* **2017**, *26*, 815–819.
- (87) Rossouw, M.; Liles, D.; Thackeray, M.; David, W.; Hull, S. Alpha Manganese Dioxide for Lithium Batteries: A Structural and Electrochemical Study. *Mater. Res. Bull.* **1992**, *27*, 221–230.
- (88) Robinson, D. M.; Go, Y. B.; Mui, M.; Gardner, G.; Zhang, Z.; Mastrogiovanni, D.; Garfunkel, E.; Li, J.; Greenblatt, M.; Dismukes, G. C. Photochemical Water Oxidation by Crystalline Polymorphs of Manganese Oxides: Structural Requirements for Catalysis. *J. Am. Chem. Soc.* **2013**, *135*, 3494–3501.
- (89) Zhou, G.; Liu, H.; Ma, Z.; Li, H.; Pei, Y. Spatially Confined Li–Oxygen Interaction in the Tunnel of  $\alpha$ -MnO<sub>2</sub> Catalyst for Li–Air Battery: A First-Principles Study. *J. Phys. Chem. C* **2017**, *121*, 16193–16200.
- (90) Li, L.; Pan, Y.; Chen, L.; Li, G. One-Dimensional  $\alpha$ -MnO<sub>2</sub>: Trapping Chemistry of Tunnel Structures, Structural Stability, and Magnetic Transitions. *J Solid State Chem* **2007**, *180*, 2896–2904.
- (91) Himmetoglu, B.; Wentzcovitch, R. M.; Cococcioni, M. First-Principles Study of Electronic and Structural Properties of CuO. *Phys. Rev. B* **2011**, *84*, 115108.
- (92) Bajaj, A.; Janet, J. P.; Kulik, H. J. Communication: Recovering the Flat-Plane Condition in Electronic Structure Theory at Semi-Local DFT Cost. *J. Chem. Phys.* **2017**, *147*, 191101.



- (93) Linscott, E. B.; Cole, D. J.; Payne, M. C.; O'Regan, D. D. Role of Spin in the Calculation of Hubbard  $U$  and Hund's  $J$  Parameters from First Principles. *Phys. Rev. B* **2018**, *98*, 235157.
- (94) Salari, H.; Kohantorabi, M. Facile Template-Free Synthesis of New  $\alpha$ -MnO<sub>2</sub> Nanorod/Silver Iodide p-n Junction Nanocomposites with High Photocatalytic Performance. *New J. Chem.* **2020**, *44*, 7401–7411.
- (95) Shah, S. I.; Khan, T.; Khan, R.; Khan, S. A.; Khattak, S. A.; Khan, G. Study of Structural, Optical and Dielectric Properties of  $\alpha$ -MnO<sub>2</sub> Nanotubes (NTS). *J. Mater. Sci. Mater. Electron.* **2019**, *30*, 19199–19205.
- (96) Ling, C.; Mizuno, F. Capture Lithium in  $\alpha$ MnO<sub>2</sub>: Insights From First Principles. *Chem. Mater.* **2012**, *24*, 3943–3951.
- (97) Ricca, C.; Timrov, I.; Cococcioni, M.; Marzari, N.; Aschauer, U. Self-Consistent Site-Dependent DFT+ $U$  Study of Stoichiometric and Defective SrMnO<sub>3</sub>. *Phys. Rev. B* **2019**, *99*, 094102.
- (98) Freysoldt, C.; Grabowski, B.; Hickel, T.; Neugebauer, T.; Kresse, G.; Janotti, A.; Van de Walle, C. First-Principles Calculations for Point Defects in Solids. *Rev. Mod. Phys.* **2014**, *86*, 253.
- (99) Hoang, K.; Johannes, M. Defect Physics in Complex Energy Materials. *J. Phys.: Condens. Matter* **2018**, *30*, 293001.
- (100) Khan, A.; Toufig, A.; Tariq, F.; Khan, Y.; Hussain, R.; Akhtar, N.; Rahman, S. Influence of Fe Doping on the Structural, Optical and Thermal Properties of  $\alpha$ -MnO<sub>2</sub> Nanowires. *Mater. Res. Express* **2019**, *6*, 065043.
- (101) Raebiger, H.; Lany, S.; Zunger, A. Charge Self-Regulation upon Changing the Oxidation State of Transition Metals in Insulators. *Nature* **2008**, *453*, 763.

- (102) Resta, R. Charge States in Transition. *Nature* **2008**, *453*, 735.
- (103) Jansen, M. and Wedig, U., A Piece of the Picture - Misunderstanding of Chemical Concepts. *Angew. Chem., Int. Ed.* **2008**, *47*, 10026.
- (104) Ku, C.; Sit, P.-L. Oxidation-State Constrained Density Functional Theory for the Study of Electron-Transfer Reactions. *J. Chem. Theory Comput.* **2019**, *15*, 4781.

# Supporting Information for Pivotal Role of Intersite Hubbard Interactions in Fe-Doped $\alpha$ -MnO<sub>2</sub>

## S1 Computational method

In this section we briefly discuss the basics of DFT+ $U+V$ <sup>1,2</sup> and of DFPT for computing Hubbard parameters.<sup>3,4</sup> All equations can be easily reduced to DFT+ $U$  by simply setting  $V = 0$ . For the sake of simplicity, the formalism is presented in the framework of norm-conserving (NC) pseudopotentials (PPs) in the collinear spin-polarized case. The generalization to the ultrasoft (US) PP and the projector augmented wave (PAW) method can be found in ref 4. Hartree atomic units are used.

### S1.1 DFT+ $U+V$

In DFT+ $U+V$ , an extended Hubbard correction energy  $E_{U+V}$  is added to the approximate DFT energy  $E_{\text{DFT}}$ :<sup>1</sup>

$$E_{\text{DFT}+U+V} = E_{\text{DFT}} + E_{U+V}. \quad (\text{S1})$$

At variance with DFT+ $U$  that contains only onsite interactions scaled by  $U$ , DFT+ $U+V$  contains also intersite interactions between an atom and its surrounding ligands scaled by  $V$ . In the case of pristine and Fe-doped  $\alpha$ -MnO<sub>2</sub>, the onsite  $U$  correction is needed for the Mn( $3d$ ) and Fe( $3d$ ) states, while the intersite  $V$  correction is used for Mn( $3d$ )–O( $2p$ ) and Fe( $3d$ )–O( $2p$ ) interactions.<sup>5</sup> In the simplified rotationally-invariant formulation<sup>6</sup> the extended Hubbard correction energy reads:

$$E_{U+V} = \frac{1}{2} \sum_I \sum_{\sigma mm'} U^I (\delta_{mm'} - n_{mm'}^{II\sigma}) n_{m'm}^{II\sigma} - \frac{1}{2} \sum_I \sum_{J(J \neq I)}^* \sum_{\sigma mm'} V^{IJ} n_{mm'}^{IJ\sigma} n_{m'm}^{JI\sigma}, \quad (\text{S2})$$

where  $I$  and  $J$  are the atomic site indices,  $m$  and  $m'$  are the magnetic quantum numbers associated with a specific angular momentum [ $l = 2$  for Mn( $3d$ ) and Fe( $3d$ ), and  $l = 1$  for O( $2p$ )],  $U^I$  and  $V^{IJ}$  are the effective onsite and intersite Hubbard parameters, and the star in the sum denotes that for each atom  $I$  the index  $J$  covers all its neighbors up to a given distance.

The generalized occupation matrices  $n_{mm'}^{IJ\sigma}$  are based on a projection of the Kohn-Sham (KS) states on localized orbitals  $\phi_m^I(\mathbf{r})$  of neighbor atoms:

$$n_{mm'}^{IJ\sigma} = \sum_{v,\mathbf{k}} f_{v,\mathbf{k}}^\sigma \langle \psi_{v,\mathbf{k}}^\sigma | \phi_{m'}^J \rangle \langle \phi_m^I | \psi_{v,\mathbf{k}}^\sigma \rangle, \quad (\text{S3})$$

where  $v$  and  $\sigma$  are the band and spin labels of the KS wavefunctions  $\psi_{v,\mathbf{k}}^\sigma(\mathbf{r})$ , respectively,  $\mathbf{k}$  indicate points in the first Brillouin zone,  $f_{v,\mathbf{k}}^\sigma$  are the occupations of the KS states, and  $\phi_m^I(\mathbf{r}) \equiv \phi_m^{\gamma(I)}(\mathbf{r} - \mathbf{R}_I)$  are the localized orbitals centered on the  $I$ th atom of type  $\gamma(I)$  at the position  $\mathbf{R}_I$ . It is convenient to establish a short-hand notation for the onsite occupation matrix:  $n_{mm'}^{I\sigma} \equiv n_{mm'}^{II\sigma}$ , which is used in the standard DFT+ $U$  approach. The two terms in Eq. (S2) (i.e., proportional to the onsite  $U^I$  and intersite  $V^{IJ}$  couplings) counteract each other: the onsite term favors localization on atomic sites (thus suppressing hybridization with neighbors), while the intersite term favors hybridized states with components on neighbor atoms. More details about DFT+ $U$ + $V$  can be found in refs 1, 7, 8. Thus, computing  $U^I$  and  $V^{IJ}$  is crucial to determine the degree of localization of  $3d$  electrons on Mn and Fe sites and the degree of hybridization of these  $3d$  electrons with  $2p$  electrons centered on neighboring O sites. In the next subsection we discuss briefly how these Hubbard parameters can be computed using DFPT.

## S1.2 Hubbard parameters from DFPT

In Hubbard-corrected DFT the values of Hubbard parameters are not known *a priori*, and hence often these values are chosen empirically such that the final results of simulations

match some experimental properties of interest. This is, though, fairly arbitrary and, hence, first-principles calculations of Hubbard parameters are essential and highly desirable. In this paper, we compute  $U$  and  $V$  from a generalized piece-wise linearity condition imposed through linear-response theory,<sup>9</sup> based on density-functional perturbation theory (DFPT).<sup>3,4</sup> DFPT has proven to be effective for determining Hubbard parameters for a variety of systems with complex magnetic properties.<sup>10–13</sup> Within this framework, the Hubbard parameters are defined as:<sup>9</sup>

$$U^I = (\chi_0^{-1} - \chi^{-1})_{II}, \quad V^{IJ} = (\chi_0^{-1} - \chi^{-1})_{IJ}, \quad (\text{S4})$$

where  $\chi_0$  and  $\chi$  are the bare and self-consistent susceptibilities which measure the response of atomic occupations to shifts in the potential acting on individual Hubbard manifolds.  $\chi$  is defined as  $\chi_{IJ} = \sum_{m\sigma} (dn_{mm}^{I\sigma}/d\alpha^J)$ , where  $\alpha^J$  is the strength of the perturbation of electronic occupations of the  $J$ th site, and it is computed at self-consistency of the DFPT calculation, while  $\chi_0$  has a similar definition but it is computed before the self-consistent re-adjustment of the Hartree and exchange-correlation potentials.<sup>3</sup> The response of the occupation matrix is computed in a unit cell as:

$$\frac{dn_{mm'}^{I\sigma}}{d\alpha^J} = \frac{1}{N_{\mathbf{q}}} \sum_{\mathbf{q}}^{N_{\mathbf{q}}} e^{i\mathbf{q}\cdot(\mathbf{R}_l - \mathbf{R}_{l'})} \Delta_{\mathbf{q}}^{s'} n_{mm'}^{s\sigma}, \quad (\text{S5})$$

where  $\mathbf{q}$  is the wavevector of the monochromatic perturbation,  $N_{\mathbf{q}}$  is the total number of  $\mathbf{q}$ 's,  $\Delta_{\mathbf{q}}^{s'} n_{mm'}^{s\sigma}$  is the lattice-periodic response of atomic occupations to a  $\mathbf{q}$ -specific monochromatic perturbation,  $I \equiv (l, s)$  and  $J \equiv (l', s')$ , where  $s$  and  $s'$  are the atomic indices in unit cells while  $l$  and  $l'$  are the unit cell indices,  $\mathbf{R}_l$  and  $\mathbf{R}_{l'}$  are the Bravais lattice vectors. The  $\mathbf{q}$  grid must be chosen dense enough to make the atomic perturbations decoupled from their periodic replicas. More details about this approach can be found in refs 3, 4. It is important to note that the main advantage of DFPT is that it does not require the usage of computationally expensive supercells contrary to the original linear-response formulation of ref 9.

Finally, it is very important to remind that the values of the computed Hubbard pa-

rameters are strongly dependent on the type of Hubbard projector functions  $\phi_m^I(\mathbf{r})$  that are used in Eq. (S3). In this work we use the atomic orbitals orthogonalized using the Löwdin method.<sup>14,15</sup> In fact, it has been shown in previous studies that Hubbard-corrected DFT with this type of Hubbard projectors and respective Hubbard parameters computed using DFPT gives an accurate description of various materials' properties.<sup>16–20</sup> In particular, in ref 21 we have shown that the most accurate description of the structural, electronic, and magnetic properties of  $\beta$ -MnO<sub>2</sub> is obtained using Löwdin-orthogonalized atomic orbitals as Hubbard projectors.

## S2 Crystal structure properties and projected density of states of the pristine $\alpha$ -MnO<sub>2</sub>

Table S1: Crystal structure parameters (CSP) of the pristine  $\alpha$ -MnO<sub>2</sub> (see Fig. 1 in the main text): lattice parameters  $a$  and  $c$  (in Å), volume  $V$  (in Å<sup>3</sup>) corresponding to the 24-atoms unit cell and its deviation  $\Delta V$  (in %) from the experimental value 274.5 Å<sup>3</sup> of ref 22. All theoretical predictions preserve the tetragonal symmetry (hence  $a = b$  and we report only  $a$ ). The results are presented for five collinear magnetic orderings (FM, A2-AFM, C-AFM, C2-AFM, and G-AFM) computed at three level of theory (see Fig. 2 in the main text): DFT, DFT+ $U$ , and DFT+ $U$ + $V$  (PBEsol functional). Hubbard-corrected results are obtained using Löwdin-orthogonalized atomic orbitals as Hubbard projector functions and the respective Hubbard parameters (see Table 1 in the main text). The experimental CSP for the pristine  $\alpha$ -MnO<sub>2</sub> (tetragonal structure) are  $a_{\text{exp}} = 9.75$  Å,  $c_{\text{exp}} = 2.86$  Å, and  $V_{\text{exp}} = 272.0$  Å<sup>3</sup> according to ref 23;  $a_{\text{exp}} = 9.84$  Å,  $c_{\text{exp}} = 2.86$  Å, and  $V_{\text{exp}} = 276.9$  Å<sup>3</sup> according to ref 24;  $a_{\text{exp}} = 9.79$  Å,  $c_{\text{exp}} = 2.86$  (2.87) Å, and  $V_{\text{exp}} = 274.1$  (274.5) Å<sup>3</sup> according to ref 22.

Magnetic ordering	CSP	DFT	DFT+ $U$	DFT+ $U$ + $V$
FM	$a$ (Å)	9.71	9.93	9.84
	$c$ (Å)	2.94	2.95	2.92
	$V$ (Å <sup>3</sup> )	267.47	291.14	282.34
	$\Delta V$ (%)	-2.56	6.06	2.86
A2-AFM	$a$ (Å)	9.71	9.86	9.81
	$c$ (Å)	2.84	2.94	2.91
	$V$ (Å <sup>3</sup> )	267.5	285.42	279.83
	$\Delta V$ (%)	-2.55	3.98	1.94
C-AFM	$a$ (Å)	9.66	9.81	9.76
	$c$ (Å)	2.83	2.93	2.90
	$V$ (Å <sup>3</sup> )	264.44	281.55	276.76
	$\Delta V$ (%)	-3.66	2.57	0.82
C2-AFM	$a$ (Å)	9.66	9.85	9.78
	$c$ (Å)	2.83	2.93	2.91
	$V$ (Å <sup>3</sup> )	263.91	284.61	278.26
	$\Delta V$ (%)	-3.86	3.68	1.37
G-AFM	$a$ (Å)	9.69	9.83	9.78
	$c$ (Å)	2.82	2.92	2.90
	$V$ (Å <sup>3</sup> )	265.16	282.57	277.41
	$\Delta V$ (%)	-3.40	2.94	1.06

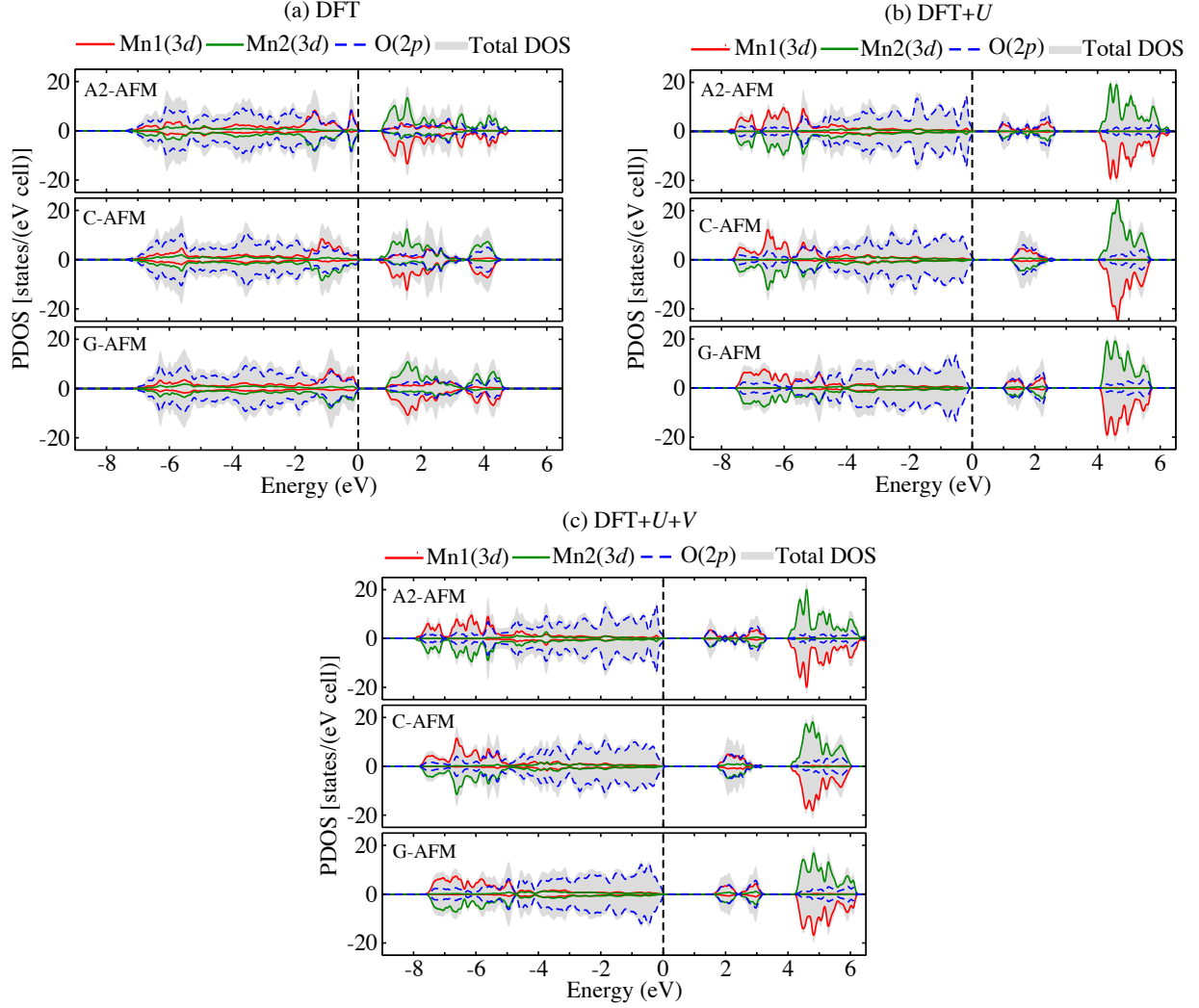


Figure S1: Spin-resolved PDOS and total DOS for the A2-AFM, C-AFM, and G-AFM magnetic orderings of the pristine  $\alpha$ -MnO<sub>2</sub> computed at three levels of theory using the PBEsol functional: (a) DFT, (b) DFT+ $U$ , and (c) DFT+ $U$ + $V$ . For each case, the Hubbard parameters  $U$  and  $V$  were computed using DFPT using Löwdin-orthogonalized atomic orbitals and are listed in Table 1 of the main text. The zero of energy corresponds to the top of the valence bands. The intensity of PDOS and total DOS was rescaled to the 24-atoms unit cell for G-AFM.



### S3 Crystal structure properties, projected density of states, population analysis for the Fe-doped $\alpha$ -MnO<sub>2</sub>

Table S2: Crystal structure parameters (CSP) of the Fe-doped  $\alpha$ -MnO<sub>2</sub>: lattice parameters  $a$ ,  $b$ , and  $c$  (in Å), angles  $\alpha$ ,  $\beta$ ,  $\gamma$  (in degrees), and the volume  $V$  (in Å<sup>3</sup>). The results are presented for five collinear magnetic orderings (A, B, C, D, and E - see Fig. 7 in the main text) computed at three level of theory: DFT, DFT+ $U$ , and DFT+ $U$ + $V$  (PBEsol functional). Hubbard-corrected results are obtained using Löwdin-orthogonalized atomic orbitals as Hubbard projector functions and the respective Hubbard parameters (see Table 3 in the main text). The experimental CSP for the Fe-doped  $\alpha$ -MnO<sub>2</sub> are  $a_{\text{exp}} = 9.83$  Å,  $b_{\text{exp}} = 9.83$  Å,  $c_{\text{exp}} = 2.86$  Å, and  $V_{\text{exp}} = 276.4$ .<sup>25</sup>

Magnetic ordering	CSP	DFT	DFT+ $U$	DFT+ $U$ + $V$
A	$a$	9.49	9.68	9.62
	$b$	9.49	9.68	9.62
	$c$	2.84	3.07	3.03
	$\alpha$	90.00	90.00	90.00
	$\beta$	90.00	90.00	90.00
	$\gamma$	90.00	90.00	90.00
	$V$	255.80	287.29	280.38
B	$a$	9.70	9.94	9.86
	$b$	9.69	9.95	9.87
	$c$	2.83	2.96	2.93
	$\alpha$	90.00	90.00	90.00
	$\beta$	90.00	90.00	90.00
	$\gamma$	89.81	89.79	89.87
	$V$	266.30	292.73	284.81
C	$a$	9.68	9.96	9.87
	$b$	9.70	9.94	9.86
	$c$	2.83	2.96	2.93
	$\alpha$	90.00	90.00	90.00
	$\beta$	90.00	90.00	90.00
	$\gamma$	90.23	90.17	90.09
	$V$	266.08	292.99	284.79
D	$a$	9.49	9.60	9.56
	$b$	9.48	9.60	9.56
	$c$	2.82	3.06	3.03
	$\alpha$	90.00	90.00	90.00
	$\beta$	90.00	90.00	90.00
	$\gamma$	89.75	89.54	89.87
	$V$	253.80	281.92	276.41
E	$a$	9.63	9.89	9.84
	$b$	9.64	9.87	9.77
	$c$	2.83	2.94	2.91
	$\alpha$	90.00	89.86	89.79
	$\beta$	90.00	89.50	89.40
	$\gamma$	90.21	90.09	89.88
	$V$	262.36	286.89	280.14

Table S3: Crystal structure parameters (CSP) for the A and D types of the Fe-doped  $\alpha$ -MnO<sub>2</sub> at the levels of DFT, DFT+ $U$ , and DFT+ $U+V$ . Bond lengths are shown for Mn–O and Fe–O couples, and the angles  $\theta_1$ – $\theta_3$  and  $\phi_1$ – $\phi_4$  are shown in Fig. S2.

CSP	A			D		
	DFT	DFT+ $U$	DFT+ $U+V$	DFT	DFT+ $U$	DFT+ $U+V$
Mn–O	1.83 – 2.00	1.86 – 2.10	1.85 – 2.09	1.81 – 2.02	1.86 – 2.13	1.85 – 2.11
Fe–O	2.18	2.16	2.17	2.16 – 2.19	2.13 – 2.21	2.13 – 2.21
$\theta_1$	130.02	127.08	127.31	130.40 – 130.41	126.69	127.07
$\theta_2$	97.87	98.90	98.77	98.34 – 98.63	98.42 – 99.04	98.51 – 99.08
$\theta_3$	90.73	89.92	90.32	90.57 – 90.78	90.48 – 91.14	90.50 – 91.13
$\phi_1$	90.00	90.00	90.00	90.07	90.14	90.05
$\phi_2$	125.07	125.20	125.16	124.12 – 125.12	125.98 – 126.43	125.73 – 126.32
$\phi_3$	124.07	124.00	123.93	124.23 – 124.61	122.91 – 123.62	123.18 – 123.73
$\phi_4$	90.00	90.00	90.00	89.93	89.86 – 89.87	89.95

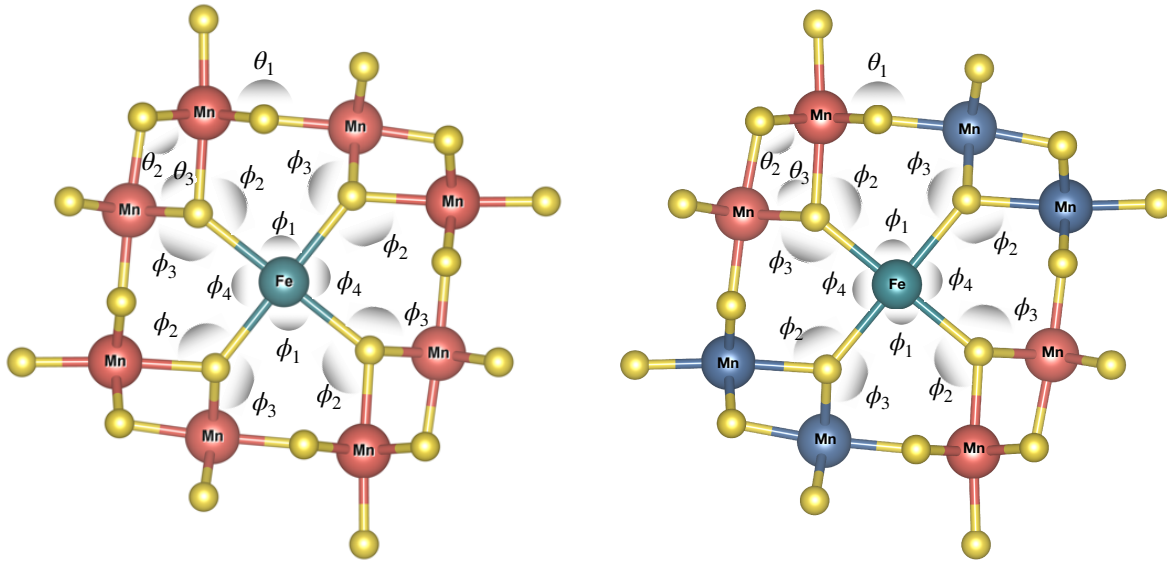


Figure S2: Bond angles in the Fe-doped  $\alpha$ -MnO<sub>2</sub> for the A type (left panel) and D type (right panel) spin configurations (see Fig. 7 in the main text). Light brown and blue colors correspond to Mn atoms with spin-up and spin-down alignments, respectively, while light green color corresponds to the Fe atom with the spin-up alignment. The oxygen atoms are shown in yellow color.

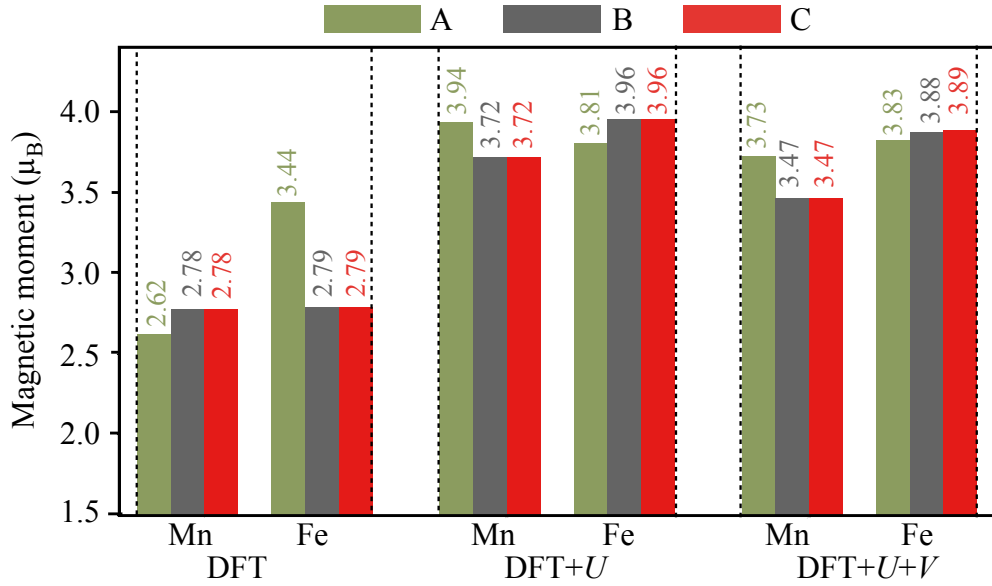


Figure S3: Magnetic moment (in  $\mu_B$ ) on Mn and Fe atoms in the Fe-doped  $\alpha$ -MnO<sub>2</sub> for three collinear magnetic orderings (A, B, and C types) computed at three levels of theory (DFT, DFT+ $U$ , and DFT+ $U$ + $V$ ) using the PBEsol functional. For each case, the Hubbard parameters  $U$  and  $V$  were computed using DFPT and are listed in Table 3 in the main text.

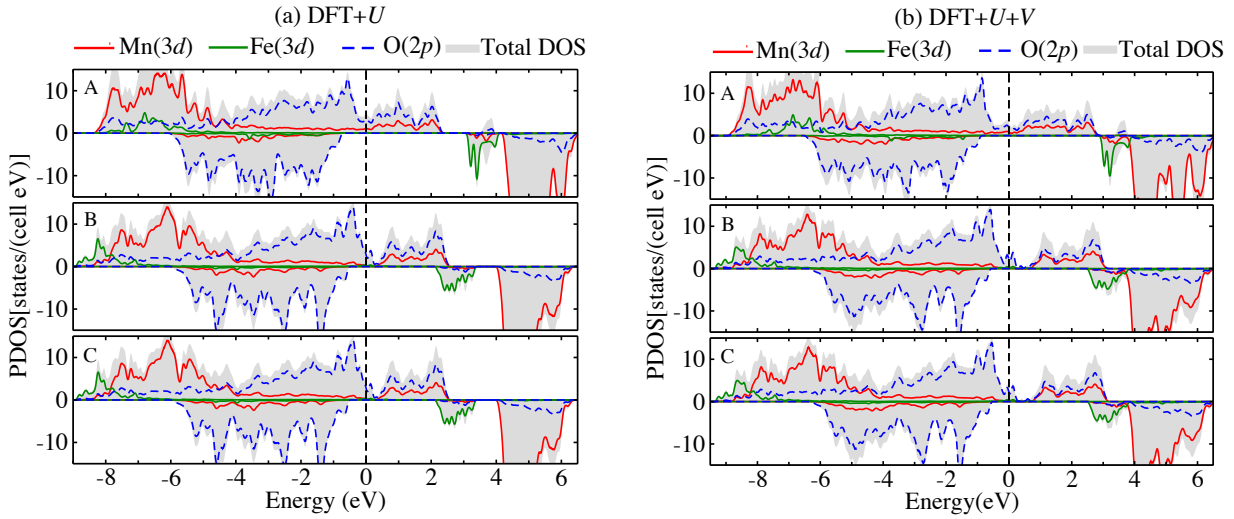


Figure S4: Spin-resolved PDOS and total DOS for three collinear magnetic orderings of the Fe-doped  $\alpha$ -MnO<sub>2</sub> (A, B, and C types) computed using the PBEsol functional within (a) DFT+ $U$ , and (b) DFT+ $U$ + $V$ . For each case the Hubbard parameters  $U$  and  $V$  were computed using DFPT and are listed in Table 3 in the main text. Upper panels correspond to the spin-up components, while lower panels correspond to the spin-down components. The zero of energy corresponds to the Fermi energy.

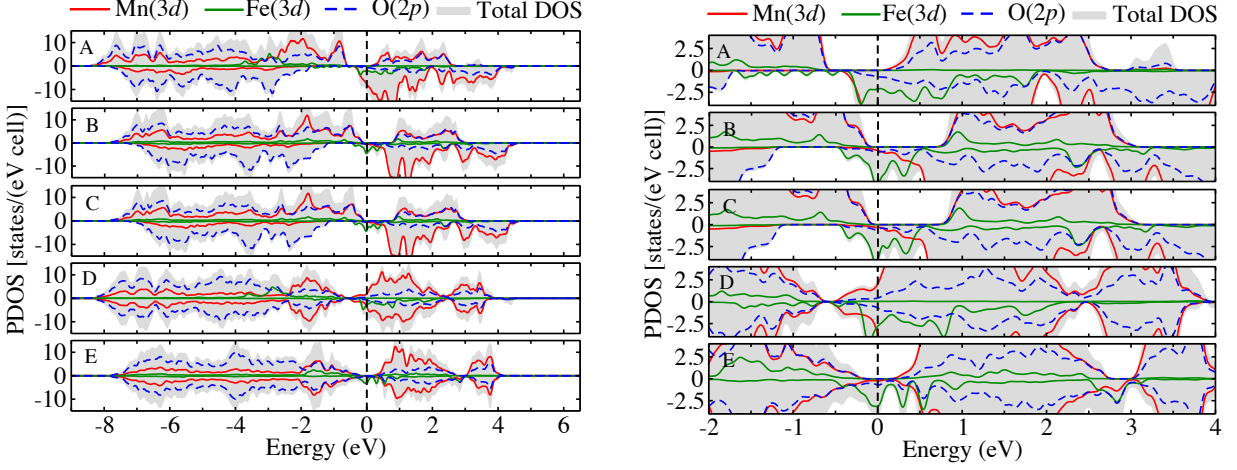


Figure S5: Spin-resolved PDOS and total DOS (left panels) and its zoom (right panels) for five collinear magnetic orderings of the Fe-doped  $\alpha$ -MnO<sub>2</sub> (A, B, C, D, and E) computed using standard DFT (PBEsol functional). The zero of energy corresponds to the Fermi energy.

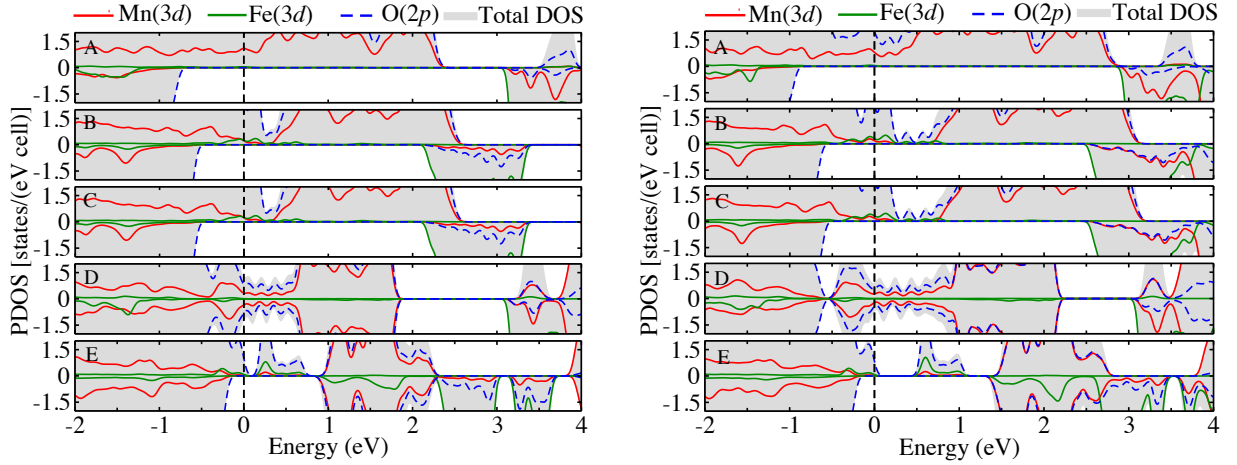


Figure S6: Zoomed-in spin-resolved PDOS and total DOS for five collinear magnetic orderings of the Fe-doped  $\alpha$ -MnO<sub>2</sub> (A, B, C, D, and E) computed using DFT+ $U$  (left panels) and DFT+ $U$ + $V$  (right panels) with the PBEsol functional. For each case, the Hubbard parameters  $U$  and  $V$  were computed using DFPT. The zero of energy corresponds to the Fermi energy (in the case of metallic ground states) or top of the valence bands (in the case of insulating ground states).

Table S4: Population analysis data for the  $3d$  shell of Mn and Fe atoms in the Fe-doped  $\alpha$ -MnO<sub>2</sub> computed using DFT+ $U$ + $V$  (PBEsol functional). Two doping types are considered: interstitial (D) and substitutional (E). This table shows the eigenvalues of the site-diagonal occupation matrix for the spin-up ( $\lambda_i^\uparrow, i = \overline{1,5}$ ) and spin-down ( $\lambda_i^\downarrow, i = \overline{1,5}$ ) channels, Löwdin occupations  $n = \sum_i(\lambda_i^\uparrow + \lambda_i^\downarrow)$ , and the oxidation state (OS). For the sake of simplicity we dropped the atomic site index  $I$  from all quantities reported here. The eigenvalues are written in the ascending order (from left to right) for each spin channel. The eigenvalues written in bold are considered as being such that correspond to fully occupied states and thus are taken into account when determining the OS according to ref 26.

Doping	Element	$\lambda_1^\uparrow$	$\lambda_2^\uparrow$	$\lambda_3^\uparrow$	$\lambda_4^\uparrow$	$\lambda_5^\uparrow$	$\lambda_1^\downarrow$	$\lambda_2^\downarrow$	$\lambda_3^\downarrow$	$\lambda_4^\downarrow$	$\lambda_5^\downarrow$	$n$	OS
D type	Mn1	0.57	0.61	<b>0.99</b>	<b>1.00</b>	<b>1.00</b>	0.06	0.09	0.11	0.27	0.29	4.99	+4
	Mn2	0.55	0.86	<b>1.00</b>	<b>1.00</b>	<b>1.00</b>	0.04	0.07	0.09	0.18	0.25	5.01	+4
	Mn3	0.55	0.86	<b>1.00</b>	<b>1.00</b>	<b>1.00</b>	0.04	0.07	0.09	0.18	0.25	5.01	+4
	Mn4	0.57	0.61	<b>0.99</b>	<b>1.00</b>	<b>1.00</b>	0.06	0.09	0.11	0.27	0.29	4.99	+4
	Mn5	0.06	0.10	0.11	0.28	0.30	0.56	0.61	<b>0.99</b>	<b>1.00</b>	<b>1.00</b>	5.00	+4
	Mn6	0.04	0.07	0.09	0.18	0.25	0.55	0.85	<b>1.00</b>	<b>1.00</b>	<b>1.00</b>	5.01	+4
	Mn7	0.06	0.10	0.11	0.28	0.30	0.56	0.61	<b>0.99</b>	<b>1.00</b>	<b>1.00</b>	5.00	+4
	Mn8	0.04	0.07	0.09	0.18	0.25	0.55	0.85	<b>1.00</b>	<b>1.00</b>	<b>1.00</b>	5.01	+4
	Fe	<b>0.97</b>	<b>0.99</b>	<b>1.00</b>	<b>1.00</b>	<b>1.00</b>	0.02	0.02	0.03	0.15	<b>0.94</b>	6.12	+2
E type	Mn1	0.58	0.59	<b>0.99</b>	<b>1.00</b>	<b>1.00</b>	0.07	0.10	0.11	0.28	0.29	5.00	+4
	Mn2	0.58	0.59	<b>0.99</b>	<b>0.99</b>	<b>1.00</b>	0.07	0.10	0.11	0.28	0.29	5.00	+4
	Mn3	0.58	0.59	<b>0.99</b>	<b>1.00</b>	<b>1.00</b>	0.07	0.10	0.11	0.28	0.29	5.00	+4
	Mn4	0.07	0.09	0.11	0.28	0.29	0.58	0.60	<b>0.99</b>	<b>1.00</b>	<b>1.00</b>	5.00	+4
	Mn5	0.07	0.10	0.11	0.29	0.29	0.58	0.59	<b>0.99</b>	<b>1.00</b>	<b>1.00</b>	5.00	+4
	Mn6	0.07	0.10	0.11	0.28	0.29	0.58	0.59	<b>0.99</b>	<b>1.00</b>	<b>1.00</b>	5.00	+4
	Mn7	0.07	0.10	0.11	0.28	0.29	0.58	0.59	<b>0.99</b>	<b>1.00</b>	<b>1.00</b>	5.00	+4
	Fe	0.78	<b>0.99</b>	<b>1.00</b>	<b>1.00</b>	<b>1.00</b>	0.09	0.12	0.18	0.30	0.37	5.80	+4

## References

- (1) Campo Jr, V. L.; Cococcioni, M. Extended DFT+ $U$ + $V$  Method with On-site and Inter-site Electronic Interactions. *J. Phys. Condens. Matter* **2010**, *22*, 055602.
- (2) Himmetoglu, B.; Floris, A.; De Gironcoli, S.; Cococcioni, M. Hubbard-Corrected DFT Energy Functionals: The LDA+ $U$  Description of Correlated Systems. *Int. J. Quant. Chem.* **2014**, *114*, 14–49.
- (3) Timrov, I.; Marzari, N.; Cococcioni, M. Hubbard Parameters from Density-Functional Perturbation Theory. *Phys. Rev. B* **2018**, *98*, 085127.
- (4) Timrov, I.; Marzari, N.; Cococcioni, M. Self-Consistent Hubbard Parameters from Density-Functional Perturbation Theory in the Ultrasoft and Projector-Augmented Wave Formulations. *Phys. Rev. B* **2021**, *103*, 045141.
- (5) Kulik, H.; Marzari, N. Transition-Metal Dioxides: A Case for the Intersite Term in Hubbard-Model Functionals. *J. Chem. Phys.* **2011**, *134*, 094103.
- (6) Dudarev, S.; Botton, G.; Savrasov, S.; Humphreys, C.; Sutton, A. Electron-Energy-Loss Spectra and the Structural Stability of Nickel Oxide: An LSDA+ $U$  Study. *Phys. Rev. B* **1998**, *57*, 1505.
- (7) Tancogne-Dejean, N.; Rubio, A. Parameter-Free Hybridlike Functional Based on an Extended Hubbard Model: DFT+ $U$ + $V$ . *Phys. Rev. B* **2020**, *102*, 155117.
- (8) Lee, S.-H.; Son, Y.-W. First-Principles Approach with a Pseudohybrid Density Functional for Extended Hubbard Interactions. *Phys. Rev. Research* **2020**, *2*, 043410.
- (9) Cococcioni, M.; de Gironcoli, S. Linear Response Approach to the Calculation of the Effective Interaction Parameters in the LDA+ $U$  Method. *Phys. Rev. B* **2005**, *71*, 035105.

- (10) Ricca, C.; Timrov, I.; Cococcioni, M.; Marzari, N.; Aschauer, U. Self-Consistent Site-Dependent DFT+ $U$  Study of Stoichiometric and Defective SrMnO<sub>3</sub>. *Phys. Rev. B* **2019**, *99*, 094102.
- (11) Floris, A.; Timrov, I.; Himmetoglu, B.; Marzari, N.; de Gironcoli, S.; Cococcioni, M. Hubbard-Corrected Density Functional Perturbation Theory with Ultrasoft Pseudopotentials. *Phys. Rev. B* **2020**, *101*, 064305.
- (12) Sun, Y.; Cococcioni, M.; Wentzcovitch, R. LDA+ $U_{sc}$  Calculations of Phase Relations in FeO. *Phys. Rev. Materials* **2020**, *4*, 063605.
- (13) Zhou, J.-J.; Park, J.; Timrov, I.; Floris, A.; Cococcioni, M.; Marzari, N.; Bernardi, M. *Ab Initio* Electron-Phonon Interactions in Correlated Electron Systems. *Phys. Rev. Lett.* **2021**, *127*, 126404.
- (14) Löwdin, P.-O. On the Non-orthogonality Problem Connected with the use of Atomic Wave Functions in the Theory of Molecules and Crystals. *J. Chem. Phys.* **1950**, *18*, 365–375.
- (15) Mayer, I. On Löwdin’s Method of Symmetric Orthogonalization. *Int. J. Quant. Chem.* **2002**, *90*, 63–65.
- (16) Ricca, C.; Timrov, I.; Cococcioni, M.; Marzari, N.; Aschauer, U. Self-Consistent DFT+ $U$ + $V$  Study of Oxygen Vacancies in SrTiO<sub>3</sub>. *Phys. Rev. Research* **2020**, *2*, 023313.
- (17) Timrov, I.; Agrawal, P.; Zhang, X.; Erat, S.; Liu, R.; Braun, A.; Cococcioni, M.; Calandra, M.; Marzari, N.; Passerone, D. Electronic Structure of Ni-Substituted LaFeO<sub>3</sub> from Near Edge X-ray Absorption Fine Structure Experiments and First-Principles Simulations. *Phys. Rev. Research* **2020**, *2*, 033265.

- (18) Kirchner-Hall, N. E.; Zhao, W.; Xiong, Y.; Timrov, I.; Dabo, I. Extensive Benchmarking of DFT+ $U$  Calculations for Predicting Band Gaps. *Appl. Sci.* **2021**, *11*, 2395.
- (19) Xiong, Y.; Campbell, Q.; Fanghanel, J.; Badding, C.; Wang, H.; Kirchner-Hall, N.; Theibault, M.; Timrov, I.; Mondschein, J.; Seth, K., et al. Optimizing Accuracy and Efficacy in Data-Driven Materials Discovery for the Solar Production of Hydrogen. *Energy Environ. Sci.* **2021**, *14*, 2335.
- (20) Timrov, I.; Aquilante, F.; Cococcioni, M.; Marzari, N. Accurate Electronic Properties and Intercalation Voltages of Olivine-type Li-ion Cathode Materials from Extended Hubbard Functionals. Cornell University, <https://arxiv.org/abs/2203.15732> (submitted March 29, 2022; accessed July 28, 2022).
- (21) Mahajan, R.; Timrov, I.; Marzari, N.; Kashyap, A. Importance of Intersite Hubbard Interactions in  $\beta$ -MnO<sub>2</sub>: A First-Principles DFT+ $U$ + $V$  Study. *Phys. Rev. Materials* **2021**, *5*, 104402.
- (22) Rossouw, M.; Liles, D.; Thackeray, M.; David, W.; Hull, S. Alpha Manganese Dioxide for Lithium Batteries: A Structural and Electrochemical Study. *Mater. Res. Bull.* **1992**, *27*, 221–230.
- (23) Thackeray, M. M. Manganese Oxides for Lithium Batteries. *Prog. Solid. State Ch.* **1997**, *25*, 1–71.
- (24) Islam, S.; Alfaruqi, M. H.; Song, J.; Kim, S.; Pham, D. T.; Jo, J.; Kim, S.; Mathew, V.; Baboo, J. P.; Xiu, Z., et al. Carbon-Coated Manganese Dioxide Nanoparticles and Their Enhanced Electrochemical Properties for Zinc-Ion Battery Applications. *J. Energy Chem.* **2017**, *26*, 815–819.
- (25) Song, L.; Duan, Y.; Cui, Y.; Huang, Z. Fe-Doped MnO<sub>2</sub> Nanostructures for Attenuation–Impedance Balance-Boosted Microwave Absorption. *ACS Appl. Nano Mater.* **2022**, *5*, 2738.



- (26) Sit, P. H.-L.; Car, R.; Cohen, M. H.; Selloni, A. Simple, Unambiguous Theoretical Approach to Oxidation State Determination via First-Principles Calculations. *Inorg. Chem.* **2011**, *50*, 10259.